Journal of Biomedical Optics

BiomedicalOptics.SPIEDigitalLibrary.org

Measurement of tissue optical properties in the context of tissue optical clearing

Alexey N. Bashkatov
Kirill V. Berezin
Konstantin N. Dvoretskiy
Maria L. Chernavina
Elina A. Genina
Vadim D. Genin
Vyacheslav I. Kochubey
Ekaterina N. Lazareva
Alexander B. Pravdin
Marina E. Shvachkina
Polina A. Timoshina
Daria K. Tuchina
Dmitry D. Yakovlev
Dmitry A. Yakovlev
Irina Yu. Yanina
Olga S. Zhernovaya
Valery V. Tuchin

Alexey N. Bashkatov, Kirill V. Berezin, Konstantin N. Dvoretskiy, Maria L. Chernavina, Elina A. Genina, Vadim D. Genin, Vyacheslav I. Kochubey, Ekaterina N. Lazareva, Alexander B. Pravdin, Marina E. Shvachkina, Polina A. Timoshina, Daria K. Tuchina, Dmitry D. Yakovlev, Dmitry A. Yakovlev, Irina Yu. Yanina, Olga S. Zhernovaya, Valery V. Tuchin, "Measurement of tissue optical properties in the context of tissue optical clearing," *J. Biomed. Opt.* **23**(9), 091416 (2018), doi: 10.1117/1.JBO.23.9.091416.

Measurement of tissue optical properties in the context of tissue optical clearing

Alexey N. Bashkatov,[a,b] Kirill V. Berezin,[a] Konstantin N. Dvoretskiy,[c] Maria L. Chernavina,[a] Elina A. Genina,[a,b] Vadim D. Genin,[a] Vyacheslav I. Kochubey,[a,b] Ekaterina N. Lazareva,[a,b,d] Alexander B. Pravdin,[a] Marina E. Shvachkina,[a] Polina A. Timoshina,[a,b] Daria K. Tuchina,[a,b,e] Dmitry D. Yakovlev,[a] Dmitry A. Yakovlev,[a] Irina Yu. Yanina,[a,b,*] Olga S. Zhernovaya,[a] and Valery V. Tuchin[a,b,f]

[a]Saratov State University, Research-Educational Institute of Optics and Biophotonics, Saratov, Russia
[b]Tomsk State University, Interdisciplinary Laboratory of Biophotonics, Tomsk, Russia
[c]Saratov State Medical University, Subdivision of Medical and Biological Physics, Saratov, Russia
[d]Immanuel Kant Baltic Federal University, Center for Functionalized Magnetic Materials, Kaliningrad, Russia
[e]Prokhorov General Physics Institute of the Russian Academy of Sciences, Moscow, Russia
[f]Institute of Precision Mechanics and Control of the Russian Academy of Sciences, Saratov, Russia

Abstract. Nowadays, dynamically developing optical (photonic) technologies play an ever-increasing role in medicine. Their adequate and effective implementation in diagnostics, surgery, and therapy needs reliable data on optical properties of human tissues, including skin. This paper presents an overview of recent results on the measurements and control of tissue optical properties. The issues reported comprise a brief review of optical properties of biological tissues and efficacy of optical clearing (OC) method in application to monitoring of diabetic complications and visualization of blood vessels and microcirculation using a number of optical imaging technologies, including spectroscopic, optical coherence tomography, and polarization- and speckle-based ones. Molecular modeling of immersion OC of skin and specific technique of OC of adipose tissue by its heating and photodynamic treatment are also discussed. [DOI: 10.1117/1.JBO.23.9.091416]

Keywords: biological tissues; skin; fat; optical properties; refractive index; optical clearing; polarization; *in vitro*; *ex vivo* and *in vivo* studies; blood vessels; microcirculation; diabetes; molecular modeling.

Paper 180089SSRR received Feb. 12, 2018; accepted for publication Jul. 30, 2018; published online Aug. 23, 2018.

1 Introduction

Recent technology advancements in photonics have spurred a prodigious progress toward the development of innovative methods and systems for clinical functional optical imaging, laser surgery, and phototherapy.[1,2] Development of optical biomedical methods and techniques has stimulated a great interest in the study of optical properties of human tissues, which define the efficacy of tissue optical probing and light action on tissue and when are known (measured) give an opportunity to predict precise photon propagation trajectories and fluence rate distribution within irradiated tissues.

Examples of application of measured tissue optical properties to diagnostics include monitoring of blood oxygenation and tissue metabolism,[3,4] imaging of skin and mucous cancer,[5,6] tracking of drug, microcontainer, and nanoparticle delivery.[7,8] In therapeutics, all kinds of treatments, such as photodynamic therapy (PDT),[9] low-level laser therapy (LLLT),[10] photothermal therapy (PTT),[11] and plasmonic photothermal therapy (PPTT),[12,13] need an accurate dosimetry that is impossible to provide without estimation of tissue optical properties. The precision of tissue laser ablation,[14] coagulation, and cutting[15,16] strongly depends on spectral properties of tissues. Therefore, for all these applications, the knowledge of tissue optical properties is of great importance for interpretation and quantification of diagnostic data and for prediction of light and absorbed energy distribution for therapeutic and surgical use. Numerous publications related to determination of tissue optical properties are available in the literature; however from year to year, the number of such studies increases. Among these studies, several books, book chapters, and reviews summarizing and analyzing data on optical properties can be mentioned.[17–26] The analysis of these publications (and references in them) shows that the optical properties of human and animal skin, subcutaneous adipose tissue (AT), breast tissue, myocardium, muscle, skull, dura mater and other brain/head tissues, maxillary sinuses, mucous membranes, stomach wall mucosa, colon, peritoneum, uterus, gallbladder, liver, aorta, lung, sclera, conjunctiva, retina and other ocular tissues, hairs, bone, cartilage, tooth enamel and dentin, and blood have been investigated in the visible- and near-infrared spectral ranges.

The investigations show a variety of advanced biomedical technologies, which are in direct need of knowledge of the optical parameters of tissues. As the most impressive and useful examples of tissue quantified data application, there are the dosimetry of radiation during PDT and PTT[27,28] and in laser surgery,[29] various imaging technologies,[1,2,19,30–40] the development of batteryless solar-powered cardiac pacemakers,[41] standardization of tissue-mimicking phantoms,[32,42–46] assessment of tissue chromophore concentration and distribution,[47,48] and proposition of adequate optical models of tissues.[49–52]

This paper gives an overview of recent results on the measurements and control of tissue optical properties that were presented on the VI International Symposium "Topical Problems of Biophotonics 2017," St.-Petersburg, Nizhny Novgorod, Russia, July 28 to August 03, 2017, as an invited talk.

*Address all correspondence to: Irina Yu. Yanina, E-mail: irina-yanina@list.ru

1083-3668/2018/$25.00 © 2018 SPIE

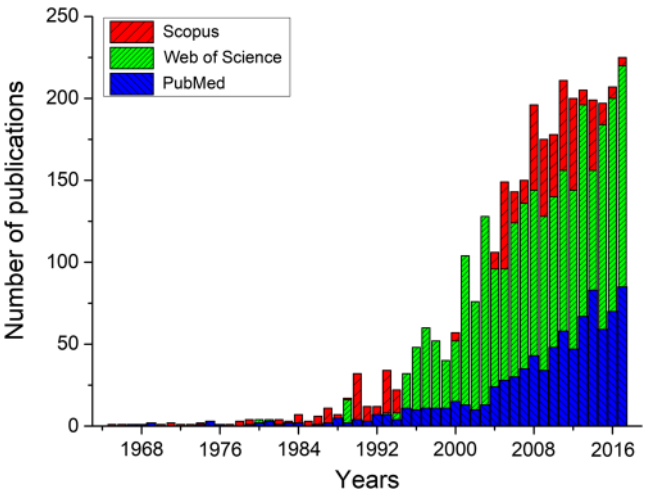

Fig. 1 Annual number of publications (over 1965 to 2017 interval) related to the measurement of tissue optical properties. Retrieved on the query "optical properties of biological tissues" from "Scopus," "Web of Science," and "PubMed" databases.

2 Optical Properties of Biological Tissues

To our knowledge, the quantitative study of optical properties of tissues began in the 50's of the last century. However, the most intensive studies have been conducted since the 90's (see Fig. 1). A rapid surge of publications during this period was caused by the development of optical technologies applicable to noninvasive or least-invasive diagnostics, therapy, and surgery of various diseases, as well as the perfection of the techniques for measurements of optical parameters of tissues in a wide wavelength range.

In the near future, a further increase in the number of publications related to the quantitative evaluation of the optical properties of not only healthy, but also pathologically modified tissues is expected, as well as the intensive use of these data for more accurate diagnosis and monitoring of malignant tumors, diabetes, cardiovascular diseases, and for dosimetry of light in PDT, LLLT, PTT, PPTT, and laser surgery.

More efficient, accurate, and fast computer algorithms and experimental methods that are already available or may appear soon will allow for the measurement of the optical properties of tissues *in vivo* in a real time. This will bring the optical method to a new horizon and significantly improve the care of people's health. For example, quantification of time varying optical parameters caused by endogenous metabolic processes or the external impact on a tissue via thermal action or due to immersion or compression optical clearing (OC)[7,17,32,53–58] will be possible.

New "tissue diagnostic/therapeutic windows" in the near-infrared (NIR) attracted a lot of attention recently.[59,60] In addition to visible (vis)/NIR "windows" such as I (625 to 975 nm), II (1100 to 1350 nm), III (1600 to 1870 nm), and IV (2100 to 2300 nm),[59,60] a narrow UV "window" (350 to 400 nm) can also be used[61] (see Fig. 2). Due to the great interest to UV,[62,63] MIR,[64–66] and terahertz[67,68] ranges in biophotonics, new studies of the optical properties of various tissues in these prospective wavelength ranges are expected to be performed soon.

In addition, as this is evident from recent publications,[69–72] one should also expect the growth in application of optical methods to characterization of tissues for the aims of food industry to test meat quality and freshness.

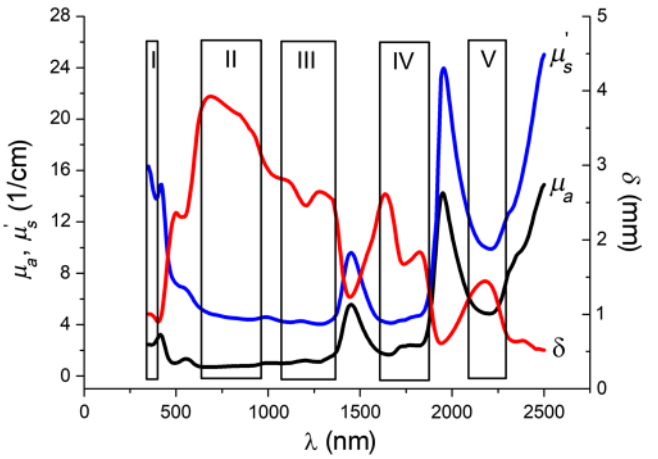

Fig. 2 Absorption (μ_a) and reduced scattering (μ_s') coefficients and light penetration depth (δ) of peritoneum[61] within tissue "optical windows" I (350 to 400 nm), II (625 to 975 nm), III (1100 to 1350 nm), IV (1600 to 1870 nm), and V (2100 to 2300 nm).

Recently, the optical properties of bovine muscle,[23] rat parietal peritoneum,[61] human[26] and rat[73] subcutaneous adipose, human skin,[26] bone,[74] stomach[75] and maxillary sinus[26] mucosa, human colon,[76] sclera,[77] and dura mater[78] were measured in the vis/NIR spectral ranges. The tissues were characterized *in vitro* using integrating sphere spectroscopy technique and inverse adding–doubling[79] or inverse Monte Carlo methods.[61,76]

Figure 3 shows absorption coefficient spectra of the tissues studied. It is well seen that tissue absorption has a minimal value in the spectral range from 600 to 1300 nm (2.5 ± 1.5 cm^{-1}), within so-called "second and third transparency windows (TW)," and from 1650 to 1800 nm (3 ± 1.5 cm^{-1}) in the "fourth-TW" of tissues. Lately, more and more interest is paid to the "fifth-TW," from 2150 to 2350 nm, with absorption coefficient of 2.5 to 15 cm^{-1}, for which scattering coefficient is the lowest. In the spectral range 400 to 600 nm, the absorption

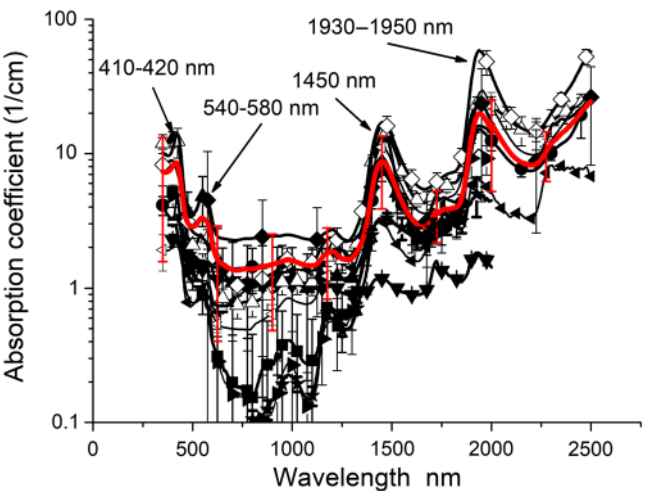

Fig. 3 Absorption spectra of human eye sclera (■),[77] skin (●),[26] AT (▼),[26] maxillary sinus (▶),[26] colon (◇),[76] stomach wall mucous (△),[75] cranial bone (ξ),[74] dura mater (□),[78] bovine muscle (▲),[23] rat parietal peritoneum (◆),[61] and rat AT (◀).[73] Red line corresponds to absorption averaged over all tissues investigated.

Table 1 The approximations for wavelength dependence of reduced scattering coefficient in the spectral range from 400 to 1300 nm for selected tissues.

Tissue	Approximation
Human eye sclera[77]	$\mu_s'(\lambda) = 1.848 \times 10^7 \lambda^{-1.995}$
Human skin[26]	$\mu_s'(\lambda) = 1.1 \times 10^{12} \lambda^{-4} + 73.7\lambda^{-0.22}$
Human subcutaneous AT[26]	$\mu_s'(\lambda) = 1050.6\lambda^{-0.68}$
Rat subcutaneous AT[73]	$\mu_s'(\lambda) = 3.017 \times 10^{10} \lambda^{-3.65} + 47.339\lambda^{-0.174}$
Human maxillary sinus mucous[26]	$\mu_s'(\lambda) = 443742.6\lambda^{-1.62}$
Human stomach wall mucous[75]	$\mu_s'(\lambda) = 3.371 \times 10^7 \lambda^{-2.305} + 20.486\lambda^{-0.141}$
Mucous layer of human colon[76]	$\mu_s'(\lambda) = 3.966 \times 10^{10} \lambda^{-3.415} + 538.08\lambda^{-0.611}$
Submucous layer of human colon[76]	$\mu_s'(\lambda) = 1.807 \times 10^{10} \lambda^{-3.488} + 561.89\lambda^{-0.754}$
Rat parietal peritoneum mucous/submucous layer[61]	$\mu_s'(\lambda) = 3.54 \times 10^{10} \lambda^{-3.531} + 28.42\lambda^{-0.124}$
Rat parietal peritoneum muscle layer[61]	$\mu_s'(\lambda) = 6.623 \times 10^{10} \lambda^{-3.964} + 44.71\lambda^{-0.393}$
Human dura mater[78]	$\mu_s'(\lambda) = 5.733 \times 10^9 \lambda^{-3.286} + 206.854\lambda^{-0.439}$
Bovine muscle[23]	$\mu_s'(\lambda) = 3.072 \times 10^{10} \lambda^{-3.407} + 8.463\lambda^{-0.09}$
Human cranial bone[74]	$\mu_s'(\lambda) = 1338\lambda^{-0.632}$

coefficient increases due to the presence of blood hemoglobin in tissues. The increase of absorption in the spectral ranges 1350 to 1600 nm, 1800 to 2150 nm, and 2350 to 2500 nm is due to the absorption of tissue water, and significant variations in absorption coefficient are connected with differences in tissue water content.

In the spectral range from 400 to 1300 nm, scattering properties of the tissues can be approximated by a power law:[21] $\mu_s'(\lambda) = \mu_s(1-g) = A\lambda^{-w_1} + B\lambda^{-w_2}$, where λ is the wavelength (nm), μ_s' is the reduced scattering coefficient (cm^{-1}), μ_s is the scattering coefficient (cm^{-1}), g is the scattering anisotropy factor, and w is the wavelength exponent. In Table 1, approximations for reduced scattering coefficient of selected tissues are summarized.

In Fig. 3 and Table 1 (see also Refs. 21 and 23), it is well seen that values of absorption and scattering coefficients for rat subcutaneous AT are larger than for human subcutaneous AT, and this difference is more noticeable within the absorption bands of lipids at the wavelengths 1720 and 1760 nm. It can be associated with the differences in structural and morphological features of these tissues. For example, in rat subcutaneous AT, the water content is about $3.5\% \pm 2.9\%$,[80] and in human, it is about 8%,[17] i.e., rat fat tissue has more structural elements (lipids, collagenous fibers, etc.) that provide larger absorption and scattering of light.

Along with integrating spheres spectroscopy, which is the most common method of *in vitro* and *ex vivo* measuring optical properties of biological tissues, optical coherence tomography (OCT) over the last decades is becoming a method of choice for *in vivo* measurements, namely scattering coefficient μ_s, anisotropy factor g, and refractive index (RI) n.[17,54,81–83] OCT has many important biomedical applications related to quantification of optical properties, such as tumor margin assessment from the surrounding healthy tissue in the course of photodynamic or photothermal treatment and in-depth monitoring of molecular diffusion in tissues.[7,17,54]

3 Refractive Index Measurements of Tissues and Blood

3.1 *Introduction*

RI of a tissue and its components is an optical parameter playing a fundamental role in light propagation in and interaction with tissues and cells as well as becoming an internal diagnostic parameter allowing for label free "optical histology."[17,84–88] Over the last decades, various techniques to determine RI of biological tissues were developed; they include confocal microscopy,[17,89] optical fiber cladding method,[90] minimal deviation angle method,[91,92] OCT with multiple modifications,[17,93–102] total internal reflection method,[88,102–106] measurement the intensity profile of diffuse light refracted into the prism around the critical angle,[107] spectroscopic refractometry,[108] and polarizing-interference microscopy.[109] The RIs of different biological tissues and cell structures can be found in Ref. 17, and some of them are presented in Table 2.[110]

The refractometric properties of biological tissues and their individual components, such as human, porcine, and rat AT, porcine muscle tissue, rat brain tissue, and the main blood proteins—hemoglobin and albumin, have been studied in a wide range of wavelengths and temperatures.[111–118] The temperature dependences of RIs were analyzed for the presence of critical points corresponding to phase transitions.

3.2 *Adipose Tissue*

Figure 4 shows temperature dependence for the mean RI for abdominal human AT measured using multiwavelength Abbe refractometer DR-M2/1550 (Atago, Japan) at 930 nm and

Table 2 RI of different tissues and cell structures. RI depends on the wavelength; here its magnitudes are given mostly for the visible range, but in some cases for a wider range from UV to NIR.[110]

	RI
Human blood plasma	1.330 ÷ 1.350
Animal cells	1.350 ÷ 1.380
Human erythrocytes	1.385 ÷ 1.392
Human blood	1.360 ÷ 1.400
Soft tissue	1.360 ÷ 1.430
Hemoglobin	1.400 ÷ 1.470
Fat	1.440 ÷ 1.510
Human dry erythrocytes	1.555 ÷ 1.567
Dry protein	1.540 ÷ 1.598

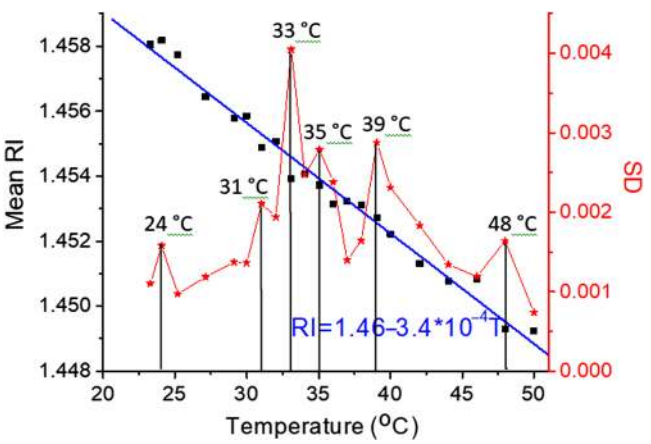

Fig. 4 Temperature dependence of mean RI measured on multiwavelength Abbe refractometer Atago at 930 nm and averaged for 10 samples of human abdominal AT [the average temperature increment is equal to $-(3.399 \times 10^{-4})°C^{-1}$ (see Table 3)]. Mean thickness of samples was 0.21 ± 0.04 mm. Bars show standard deviations (SDs). Blue line is linear approximation ($R = -0.99$). Figure is adapted from Ref. 114.

averaged for 10 samples. Mean sample thickness was 0.21 ± 0.04 mm.

The data in Table 3 can be used in extrapolating RI of the melted and sliced porcine AT for the temperatures from 25°C to 50°C, as well as RI of human sliced AT for the temperatures from 23°C to 50°C, according to

$$n(T) = n_0 + (\mathrm{d}n/\mathrm{d}T)T, \tag{1}$$

where n_0 is the RI for temperature of 0°C; $\mathrm{d}n/\mathrm{d}T$ is the temperature increment, $°C^{-1}$; and T is the current temperature, °C.[111,112,114,115,119]

The average across all wavelengths from 480 to 1550 nm RI temperature increment $\mathrm{d}n/\mathrm{d}T$ equals to $-(3.54 \pm 0.15) \times 10^{-4}°C^{-1}$ with $n_0 = 1.4833$ (see Table 3) that correlates well with the slope measured for oleic acid, $-3.8 \times 10^{-4}°C^{-1}$ with $n_0 = 1.467$.[117] This can be explained by the high content of oleic acid in human fat (46%) and its low-melting temperature (16°C).[118] Therefore, it may easily and intensively leak out from the adipose cells and accumulate at the interface between the sample and measuring prism of the refractometer.[114]

Table 4 shows mean value and SD of phase transition characteristic temperatures averaged over 10 human and 10 porcine fat samples studied using Abbe refractometer.[115]

For human fat, the very low temperature (24.1°C) and low-temperature transitions (31°C to 35°C) could be associated with the fusible free fatty acid (FFA) of a fat droplet like oleic acid; the middle temperature (39.1°C)—with cell membrane phospholipids, and the high temperature (48.0°C)—with less fusible free fatty triglyceride (FFT) of a fat droplet like palmitic acid. For porcine fat, a similar grade of phase transitions is seen, but with some difference of characteristic temperatures, which should be related to variations in composition of these two tissues. The overall analysis of 20 (10 human and 10 porcine) samples demonstrates for 12 samples the existence of very-low-temperature transitions in the range from 24.1°C to 25.5°C detected by the same measurement technique. The low-temperature transitions that are in the range from 31.0°C to 35.1°C were detected for all 20 samples, whereas the middle-temperature range transitions were found very close to each other, as (39.1 ± 0.1)°C for 10 human and (39.5 ± 1.9)°C for 9 porcine samples, with the additional transition at (44.4 ± 0.6)°C for only 6 porcine samples. The high-temperature transitions were also found to be close to each other for human and porcine AT at (48.0 ± 0.04)°C for 10 human and (50.2 ± 1.0)°C for 6 porcine samples, as only 5 porcine samples showed the additional phase transition at (55.5 ± 1.6)°C.

3.3 *Muscle Tissue*

RI is the key parameter for tissue OC, which is used to increase the imaging depth and improve the quality of images for various techniques, such as OCT, fluorescent, and many other microscopies.[17,120–122] Oliveira et al.[121] proposed an indirect method for evaluation of RI of the interstitial space of tissues, which is based on the analysis of temporal efficiency of tissue OC and was successfully tested for skeletal muscle with glucose (40%) and ethylene glycol (EG) (99%) solutions as optical clearing agents (OCAs). The method is simple, as it is based only on the measurements of time dependences of tissue sample collimated transmittance $T_c(t)$ and thickness $d(t)$ with minor calculations. Since the method uses the concept of RI matching of tissue cellular structures and controlled interstitial fluid (ISF), the refraction and structural properties of tissue components can be evaluated, as refraction, viscous, and osmotic properties of probing OCAs are known or can be measured independently with a high precision. By this method, the occurrence of the RI matching mechanism of OC was also proved.[121] This method can be applied to a variety of biological tissues at interaction with an appropriate OCA as a probe.

Highly concentrated albumin solutions can be used as the OCAs for immersion OC of muscle tissue, since their RI is close to the RI of cellular structures of tissues. Figures 5 and 6 show efficiency of OC of porcine muscle tissue immersed in 70% bovine serum albumin solution. The collimated transmittance spectra $T_c(\lambda)$ of a tissue sample were measured using a multichannel spectrometer NIRQuest 512-2.2 (Ocean Optics, USA). The tissue sample was fixed on 3.5×1.5 cm^2 plastic plate against 8×8 mm^2 hole in the center and placed in

Table 3 The initial (room temperature) values and the temperature RI increments of the melted (mp) and sliced porcine (sp) AT for the temperature range from 25°C to 50°C and sliced human (sh) AT for the temperature range from 23°C to 50°C measured using multiwavelength Abbe refractometer.[114] SD is standard deviation.

λ (nm)	$(n_0)_{mp}$ (SD)	$(dn/dT)_{mp}$ (SD), -10^{-4}°C^{-1}	$(n_0)_{sp}$ (SD)	$(dn/dT)_{sp}$ (SD), -10^{-4}°C^{-1}	$(n_0)_{sh}$ (SD)	$(dn/dT)_{sh}$ (SD), -10^{-4}°C^{-1}
480	1.4918 (0.0009)	5.870 (0.227)	1.5014 (0.0020)	7.996 (0.535)	1.4833 (0.0003)	3.777 (0.090)
589	1.4837 (0.0010)	5.698 (0.256)	1.4887 (0.0017)	6.974 (0.454)	1.4759 (0.0002)	3.604 (0.048)
680	1.4801 (0.0011)	5.923 (0.283)	1.4865 (0.0022)	7.578 (0.571)	1.4714 (0.0002)	3.576 (0.061)
930	1.4774 (0.0011)	6.028 (0.286)	1.4845 (0.0014)	7.867 (0.362)	1.4658 (0.0003)	3.399 (0.099)
1100	1.4747 (0.0011)	5.918 (0.275)	1.4806 (0.0015)	7.681 (0.397)	1.4627 (0.0003)	3.344 (0.091)
1300	1.4705 (0.0012)	6.174 (0.328)	1.4773 (0.0015)	7.990 (0.385)	1.4588 (0.0003)	3.599 (0.086)
1550	1.4685 (0.0015)	6.681 (0.405)	1.4799 (0.0022)	9.583 (0.566)	1.4539 (0.0005)	3.451 (0.148)

Table 4 Mean values and SD of phase transition temperatures found for 10 human and 10 porcine fat samples studied using Abbe refractometer[115]; SD presents temperature interval for a particular phase transition found for *N* samples; *N* is the number of samples for which a particular phase transition was observed for each series of samples.

	Phase transition temperature (mean ± SD) °C			
Transition	Human	*N*	Porcine[115]	*N*
Very low temperature	24.1 ± 0.2	For 3	25.5 ± 1.9	For 9
Low temperature	31.0 ± 0.1	For all 10	—	—
	33.1 ± 0.1	For all 10	34.1 ± 2.8	For all 10
	35.1 ± 0.1	For all 10	—	—
Middle temperature	39.1 ± 0.1	For all 10	39.5 ± 1.9	For 9
	—	—	44.4 ± 0.6	For 6
High temperature	48.0 ± 0.04	For all 10	50.2 ± 1.0	For 6
	—	—	55.5 ± 1.6	For 5

a 5-ml glass cuvette with 70% bovine albumin solution. The source of radiation was a halogen lamp HL-2000 (Ocean Optics, USA). Table 5 shows the RI values for the slice of porcine muscle tissue before and after immersion in 70% bovine albumin solution and OC efficiency. RI was measured using multiwavelength Abbe refractometer DR-M2/1550 (Atago, Japan) at 930, 1100, 1300, and 1550 nm. The efficiency of optical clearing (EOC) at 930 nm for the porcine muscle tissue after immersion was 1.56, and the RI of the sample increased from 1.3567 to 1.3777. Mean sample thickness was 1.23 ± 0.05 mm before and 1.36 ± 0.05 mm after immersion, which indicates the swelling of the tissue during experiment.

3.4 *Blood and Its Components*

Since blood contains hemoglobin, one of the major chromophores of soft tissues in the visible/NIR region, it is of great

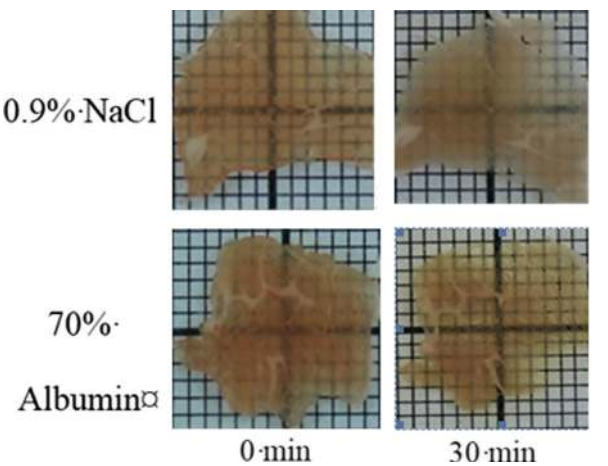

Fig. 5 Images of porcine muscle tissue samples before and after immersion in 0.9% NaCl and in 70% bovine albumin solution.

importance to know the optical properties of both whole blood and its components.[113,114,123–125] Measurement of RI of blood is of interest for many fields of optical biomedical diagnostics, including optical tomography and biopsy.[82] In the recent pilot study,[112] the possibility of detection of the critical temperatures that correspond to phase transitions of hemoglobin solutions with temperature increase was demonstrated via RI measurements. It is well known that RI of a hemoglobin solution depends linearly on temperature [see Eq. (1)] and concentration

$$n(C) = n_{H_2O} + \alpha C, \tag{2}$$

where n_{H_2O} is the RI of distilled water; C is the hemoglobin concentration; α is the specific refraction increment (see Table 6);[92,113,119] and dispersion is well described by Sellmeier equation:[113,114,126]

$$n^2(\lambda) = 1 + \frac{A_1\lambda^2}{\lambda^2 - B_1} + \frac{A_2\lambda^2}{\lambda^2 - B_2}, \tag{3}$$

where A_1, A_2, B_1, and B_2 are the empirical constants (see Table 7).

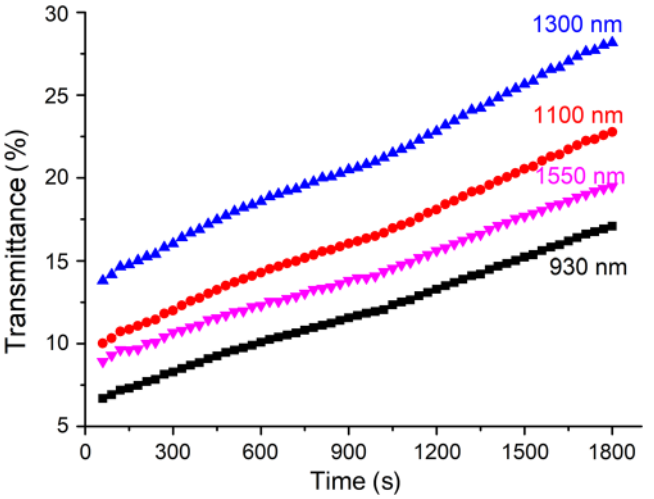

Fig. 6 Collimated transmittance at 930, 1100, 1300, and 1550 nm of (1.23 ± 0.05)-mm-thick porcine muscle sample before and (1.36 ± 0.05)-mm after immersed in 70% bovine albumin solution.

The results of RI measurements and evaluation of specific increment, temperature increment, and coefficients of Sellmeier dispersion equation for human hemoglobin and albumin are presented in Tables 6 and 7. RI was measured using a multiwavelength Abbe refractometer DR-M2/1550 (Atago, Japan) within 480 to 1550 nm spectral range for the temperature from 23 for hemoglobin and from 24 for albumin to 50°C with 1°C step. The hemoglobin solution was obtained from whole blood by hemolysis after its decomposition into fractions. The albumin solution was prepared from dry human serum albumin (Sigma Aldrich, USA). Tables 6 and 7 show the average values of RI for 10 samples of hemoglobin solution and 5 samples of albumin solution.

The refractometric method allows for quick and easy evaluation of optical properties of biological tissues and well complements other research methods, e.g., tissue OC, as it was discussed in this section.

The possibility of implementation of the refractometric method for revealing critical temperatures corresponding to phase transitions in tissues and cell structures was also demonstrated on the examples of human and porcine ATs. The obtained data for RI and its temperature increments for AT,

Table 5 The RI values for the slice of porcine muscle tissue before and after immersion in 70% bovine albumin solution and the EOC after 30 min immersion

Wavelength (nm)	RI (albumin)	RI (tissue)		EOC $\frac{T_c(30\ \text{min})-T_c(0)}{T_c(0)}$
		Before immersion	After immersion	
930	1.3990 (0.0006)	1.3567 (0.0005)	1.3777 (0.0006)	1.56
1100	1.3965 (0.0004)	1.3512 (0.0004)	1.3741 (0.0008)	1.27
1300	1.3917 (0.0002)	1.3470 (0.0006)	1.3687 (0.0002)	1.04
1550	1.3885 (0.0002)	1.3436 (0.0005)	1.3626 (0.0015)	1.18

Table 6 RI of human hemoglobin (260 g/l) and albumin (55 g/l) solutions, specific increment (α), and temperature increment (dn/dT)[112,113,116]

Wavelength (nm)	Hemoglobin			Albumin		
	RI ($T = 23$°C)	α, ml/g ($T = 23$°C)	dn/dT, -10^{-4}°C^{-1}	RI ($T = 24$°C)	α, ml/g ($T = 24$°C)	dn/dT, -10^{-4}°C^{-1}
480	1.3879	0.199	2.101	1.3480	0.184	1.103
546	1.3836	0.193	1.741	1.3449	0.173	1.139
589	1.3821	0.192	1.865	1.3434	0.168	1.297
656	1.3792	0.190	1.871	1.3414	0.174	1.164
680	1.3771	0.185	1.785	1.3405	0.174	1.088
930	1.3735	0.183	1.757	1.3361	0.158	1.073
1100	1.3690	0.183	1.766	1.3325	0.172	0.974
1300	1.3642	0.185	1.921	1.3285	0.143	0.919
1550	1.3598	0.179	1.921	1.3239	0.205	0.830

Table 7 Coefficients of Sellmeier dispersion equation for human hemoglobin (260 g/l) and albumin (55 g/l) solutions[112,113,116]

Solution	T (°C)	A_1	A_2	B_1 (nm^{-2})	B_2 (10^7 nm^{-2})	R^2
Hemoglobin	23	0.88871	190.95319	10187.17167	1039.98	0.993
	36	0.87297	576.33012	9301.83772	2914.62	0.996
	50	0.86774	691.36862	8905.96301	3389.47	0.994
Albumin	24	0.78808	0.11665	8944.13511	0.96831	0.998
	36	0.78338	0.11395	9045.64054	0.96918	0.997
	50	0.78284	0.17913	8654.84831	1.32953	0.996

human hemoglobin, and albumin are the new data supplementary to the data available in the literature.[17,87,103,123]

It is important to note that in addition to classical refractometry, the spatially resolved phase imaging methods allowing for quantitative determination of RI distribution in tissues and cells are rapidly developing.[127] They are based on the measurement of the complex field associated with high-resolution microscopic images of tissue slices, extraction the scattering coefficients and anisotropies, which enables access to tissue structural information. Many studies demonstrate the prospects of quantitative phase imaging techniques for the label-free tissue imaging and ability of diagnosis of brain, breast, and prostate cancer as well as detection of brain tissue structural alterations in Alzheimer's disease.[127–129]

3.5 *Collagenous Tissues*

The development of reliable theoretical models describing light propagation in fibrous tissues and the processes associated with the control of their optical properties is still an urgent problem.[130–137] The optical behavior of such tissues as dermis, sclera, cartilage, and tendon, as well as the walls of arteries and veins, is largely determined by the optical behavior of collagen fibers. Therefore, when considering these tissues, an adequate description of the optics of collagen bundles and processes occurring in them under the influence of external factors is of fundamental importance. A convenient model object for experimental studies of physical and physiological properties of collagen fibers is rat tail tendon (RTT) fascicles (due to their relatively simple structure, ease of extraction and manipulation, and ready availability). Fascicles are secondary collagen bundles of tendons.[138–140] Their composition and collagen fibril packing are similar to those of collagen fibers of dermis and sclera.[141] But fascicles, whose diameter typically lies within the range from 250 to 500 μm, are ten times thicker than dermal and scleral collagen bundles, which makes them quite convenient for study. An extensive series of experiments with RTT fascicles, aimed at clarifying the mechanisms of immersion OC of collagenous tissues was recently completed.[17] The application of immersion agents to RTT fascicle significantly changes not only scattering properties of the tissue, but also its birefringence and diattenuation (see example in Fig. 7), which allows for obtaining extended information about the processes occurring. The results on immersion clearing will be presented elsewhere. Here, the results of some auxiliary measurements[142] concerning the effect of water content, one of the most variable and important tissue characteristics, on the optical properties of collagen fibers, namely, on the average RI, and the average birefringence index of the tissue should be mentioned. As far as we are aware, of collagenous tissues, reliable estimates of the average RI as a function of water content were earlier obtained only for cornea,[143] which is a tissue with a very high water content.

In order to determine the average RI of RTT fascicles as a function of water content, the cross-sectional area and average RI of RTT fascicle specimens were monitored using OCT during their air-drying from the native state to the air-dry state and in the process of rehydration of dried specimens in normal saline solution (NSS: aqueous solution of 0.9 wt. % NaCl). The experimental technique is described in detail in Ref. 142; here only the main steps are outlined.

Fascicles were excised from the tails of mature rats within 1 h after decapitation, then immediately immersed in NSS. All refractive-index measurements were performed on fascicles ranging in diameter from 300 to 400 μm. The storage time of samples in NSS before they were used in experiments did not exceed 7 days. No statistically significant change (Friedman test, probability value $p = 0.32$) in the average RI of RTT fascicle specimens was observed during 7-day storage in NSS. The fascicles were mounted in a slightly stretched state on an object-plate using binder clips and covered with a cover slip.

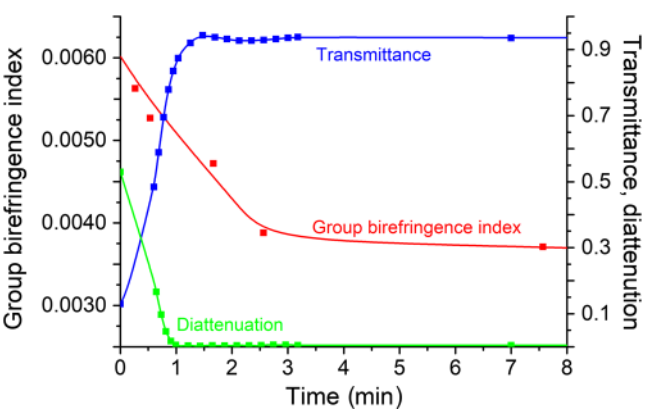

Fig. 7 Typical kinetics of the collimated transmittance, diattenuation, and average group birefringence index of RTT fascicles in the process of their OC in an 85 vol% aqueous glycerol solution. The data were obtained for different samples of similar sizes. The transmittance and diattenuation (for the same sample) were measured using polarized optical microscopy (wavelength $\lambda = 544$ nm). The average group birefringence index was measured using OCT (center wavelength $\lambda_c = 930$ nm).

In the measurements, an OCT-system ThorLabs-OCP930SR with a center wavelength (λ_c) of 930 nm was used. To estimate the average group RI n_g of the tissue using OCT, a common method was employed,[93,143–145] in which the group RI and physical thickness of the sample are determined from the measured values of the optical path length and shift of the image of a reflecting surface arranged beyond the sample with respect to its position in the absence of the sample [in our experimental geometry, as in Ref. 145, the role of this reflecting surface was played by the frontal surface of the object–plate (glass substrate); see inset in Fig. 8]. The group RI of the surrounding medium was calculated from dispersion data for the phase RI of the medium. To determine the water volume fraction C_w, the cross-sectional area of the fascicle by scaling the area of the specimen cross section in the OCT-image was first calculated using the measured group RI. Then the coefficient of fascicle volume change (volume factor), $k_s = V/V_0$, where V is the current value of tissue volume and V_0 is the volume of the tissue in the initial state, was computed. Since in our experiments the length of the fascicle did not change during both the dehydration and following rehydration, the volume factor was calculated as $k_s = S/S_0$, where S and S_0 are the current and initial values of the cross-sectional area, respectively. Finally, the water volume fraction was estimated by the equation $C_w \approx (k_s - k_{sdry})/k_s$, where k_{sdry} is the value of k_s for the dry state.

Figure 8 shows the measured dependences of the average group RI n_g on the water volume fraction C_w for four samples of RTT fascicles, samples 1, 2, 3, and 4. The OCT data for sample 1 were collected during 30 min when this sample was dried at room temperature. Sample 2 was dried at room temperature for 2 h, then held for 1 h at 50°C, and finally held for 1 h at 105°C. Sample 3 was dried for 40 min at room temperature and then for 1 h at 105°C. Sample 4 was first dried at room temperature for 20 min and then placed in NSS for rehydration. From Fig. 8, it can be seen that the data for different samples are in good agreement, as are the data for drying and rehydration of sample 4. The experimental data for bovine cornea from Ref. 143 were also transferred to Fig. 8 for comparison. It can be seen that the data for tendon and cornea fit rather well.

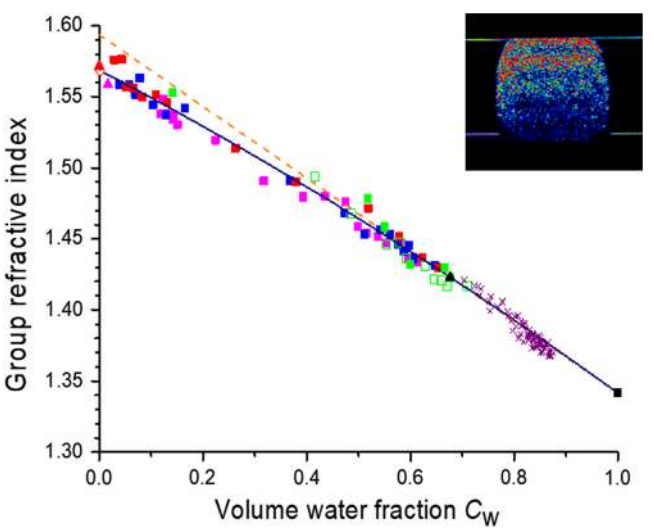

Fig. 8 Average group RI of RTT fascicles versus volume water content C_w; $\lambda_c = 930$ nm. The blue squares show experimental points (k_s, n_g) for sample 1 (air-dried at room temperature). The red symbols represent the data for sample 2: the squares are the points obtained during air-drying at room temperature; the open circle and solid triangle show the points obtained on air-drying at 50 °C and 105 °C, respectively. Purple symbols show the data for sample 3: the squares are for air-drying at room temperature, and the triangle is for air-drying at 105 °C. The green symbols are for sample 4: the solid squares are for the stage of air-drying, and open squares are for the stage of rehydration (80 min). The black triangle shows the average value of n_g of RTT fascicles in the native state (over 12 specimens). The crosses represent the experimental points for bovine cornea[143] ($\lambda_c = 819.9$ nm). The solid line represents the approximating quadratic polynomial to the data for RTT. The red dashed line is the straight line passing through the points $(C_w, n_g) = (1, 1.3416)$ (water) and (0.677, 1.423) (the average for the native state of RTT).[142]

An average value of n_g for RTT fascicles in the native state was found to be 1.423 ± 0.003. This value is shown by the black triangle in Fig. 8. The experimental data for RTT were shown to be well approximated by the quadratic polynomial $n_g = 1.5713 - 0.1969C_w - 0.0328C_w^2$ (Fig. 8). It is noteworthy that the approximation of the RTT data by the straight line passing through the points $(C_w, n_g) = (1, 1.3416)$ (water; the value 1.3416 of the group RI of water was obtained using the dispersion data for the phase RI of water of Ref. 146 and is close to the values 1.3405 ± 0.0003 and 1.3404 corresponding to dispersion data sets presented in Refs. 91 and 147, respectively) and (0.677, 1.423) (native state), the red line in Fig. 8, ensures a rather good accuracy for the range $0.52 \le C_w \le 1$ but gives a significantly overestimated value for the dry state (1.594). The significant deviation of the actual $n_g(C_w)$ curve from this approximating line in the region $C_w \le 0.52$ may be attributed to a change of the mode of hydration. In the literature, two modes of collagenous tissue hydration are distinguished.[148–151] For relatively high values of hydration parameter H, which is defined as the ratio of the weight of water to the dry weight, changes in the total water content in the tissue lead to changes of the water content in extrafibrillar space while the water content in collagen fibrils remains unchanged.[143,148–152] In the alternative mode ($H < H_c$, where H_c is a critical value, the so-called fibrillar saturation point[150]), changes in the total water content are accompanied by changes in water content both in collagen fibrils and extrafibrillar space.[148–151] For RTT, $H_c \approx 0.82$,[150,152] which corresponds to $C_w \approx 0.52$.

The average group birefringence index is usually measured using polarization-sensitive OCT systems. However, the OCT-system ThorLabs-OCP930SR used in the measurements was also found suitable for this purpose, since the probe beam was partially linearly polarized with a relatively high degree of polarization (~0.89) and the plane of polarization of the polarized component of the probe beam made an angle of 45 deg with the B-scan plane. Due to this, when the direction of the fascicle (the preferred optic axis direction) was perpendicular to the B-scan plane, interference fringes caused by the tissue birefringence were observed in OCT images (see the inset in Fig. 8). From these fringes, the average group birefringence index of the tendon was calculated. In Fig. 9, the measured values of the average group birefringence index for RTT are plotted against the volume water fraction C_w.

4 Efficacy of Optical Clearing Agents and Diffusion Coefficient

Analysis of data bases Web of Science, Scopus, and PubMed shows that the interest to the OC methods is permanently growing, which is caused by the progress of optical and laser technologies translation to biology and medicine.[54] The optical immersion clearing is based on the impregnation of a tissue

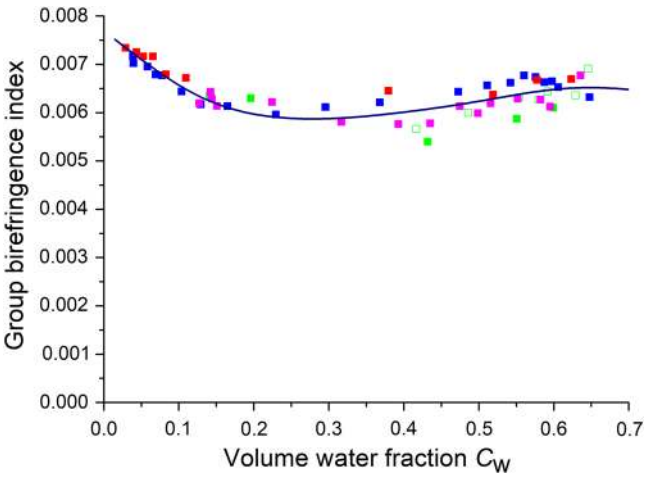

Fig. 9 Average group birefringence index of RTT fascicles versus volume water content C_w; $\lambda_c = 930$ nm. The symbols are the same as in Fig. 8.

by a biocompatible OCA with RI value close to the RI of tissue scatterers to reach an RI matching effect; these agents are often have hyperosmotic properties causing tissue temporal dehydration, less thickness of the tissue layer, and better spatial correlation between scatterers.[17,53–57] At present, different OCAs, including the solutions of sugars, polyhydric alcohols, acids, and others,[17,53,122,153–156] are used. They are biocompatible, possess sufficiently high RI, and provide effective OC of skin and other tissues.

Nowadays, the data on optical efficiency of different OCAs to select the most suitable for use in a particular case are urgently needed.[122,153–157] This section summaries studies on OC of some tissues provided by the widely used OCAs.

As OCAs dehydrated glycerol (G) and aqueous glycerol solutions with concentration from 30% to 85%, propylene glycol (PG), EG, polyethylene glycol (PEG) with MW 300 Da (PEG-300) and 400 Da (PEG-400), 1,3-butanediol (1,3-BD) and 1,4-butanediol (1,4-BD), 2-methyl-1,3-propanediol (MPD), dimethyl sulphoxide (DMSO), aqueous glucose solutions (Gl) with weight/volume concentrations from 20% to 56%, and mannitol 16% (M16) are used. The RI of the agents measured at 589 nm, their molecular weight, and dynamic viscosity obtained from literature are presented in Table 8.

OC of skin was studied for white laboratory rat and murine *ex vivo* and for human skin, rat skeletal muscle, porcine myocardium, human cranial bone, and dura mater—*in vitro*. For measuring the collimated transmittance of the samples, commercially available vis-NIR spectrometers connected to PC was used. Diffuse reflectance and total light transmittance of skin samples were measured using commercially available integrating sphere spectrometers. All measurements were performed at room temperature (~20°C).

The EOC is the parameter that allows one to compare different OCAs by their relative effect on tissue transparency. EOC was introduced in different ways, e.g., as a ratio of reduced scattering coefficient values before and after immersion during some reasonable time interval;[159] a ratio of achieved maximal collimated optical transmittance to the initial one,[168] or similar ratio, but for total transmittance;[169] the maximal resolution of the test-object visualized through a tissue sample *in vitro*, and the relative change of the parameter characterizing the signal-to-noise ratio obtained at analysis of laser speckle contrast *in vivo*.[170]

The evaluation of efficiency as a related difference of maximal and minimal values of collimated transmittance allows for obtaining the degree of skin transparency without taking into account the changes in structural properties of the tissue. However, it was shown[122,156,157,163] that alcohols and sugar solutions cause tissue shrinkage, thus corresponding decrease of sample thickness additionally contributes to the collimated transmittance increase.

The EOC evaluation using μ_s (or μ_s') allows for obtaining objective information on the change of scattering properties of the samples due to OCA immersion, since it takes into account the sample thickness variation under the action of OCAs. Thus the EOC can be evaluated using the expression:

$$\Delta^{\mu_s} = \frac{\mu_s(t=0) - \mu_{s\,\min}}{\mu_s(t=0)} \times 100\%, \tag{4}$$

where $\mu_s\ (t=0)$ is the initial scattering coefficient for the intact tissue sample and $\mu_{s\,\min}$ is the minimal value of scattering coefficient.

The knowledge of diffusion rate of OCAs is very important for the development of mathematical models describing the interaction of OCAs with tissues and creating models for effective drug delivery. The optical method of evaluation of OCA diffusion coefficient in a tissue is based on the measurements of temporal changes of tissue scattering properties.[171]

However, in the analysis of penetration of high-concentrated substances into tissues, one can consider only the relative diffusion coefficient. The relative diffusion coefficient characterizes the mean rate of the exchange fluxes of an OCA into the tissue and water out of the tissue. The analysis of collimated transmittance kinetics of the skin samples immersed in the OCA allows for estimation the relative diffusion coefficient of the OCA.[171]

The values of diffusion coefficient and EOC have been calculated for each wavelength and then averaged. Table 8 shows these values for EOC in the spectral range from 400 to 1000 nm evaluated from the literature data and diffusion coefficients of the OCAs in tissues measured *ex vivo* and *in vitro*.

One can see that dehydrated glycerol is not the most effective OCA, although it has maximal value of RI. It may be caused by high viscosity of glycerol, which prevents easy penetration of glycerol into tissue. In addition, glycerol desiccates the samples making them denser; this also prevents glycerol penetration into the tissue. The features of glycerol–collagen molecular interaction are the cause of more effective skin OC with G60 than with G85. As it follows from the results presented, PEG-400 appeared to be the most effective OCA.

Table 8 shows that dehydrated glycerol has maximal value of relative diffusion coefficient. In this case, the main contribution to the OC is made by dehydration of tissue sample, i.e., diffusivity kinetics is mostly defined by a fast water outflow.

Presented data have shown that relative changes of tissue scattering properties makes it possible to evaluate the OCA efficiency in spite of the differences in tissue sample thickness. Determination of the relative diffusion coefficient of an OCA allows for revealing the rate of OC process.

Table 8 Properties of the OCAs [molecular weight (MW), dynamic viscosity (V), RI, measured at the wavelength 589 nm], their efficiency and diffusion coefficient in tissues. Glycerol (G), propyleneglycol (PG), ethyleneglycol (EG), polyethylene glycol (PEG), 1,3-butanediol (1,3-BD), 1,4-butanediol (1,4-BD), 2-methyl-1,3-propanediol (MPD), dimethylsulphoxide (DMSO), glucose solutions (Gl), and mannitol 16% (M16).

OCA	MW (Da)	V (mPa × s)	RI	Efficiency (%)	Diffusion coefficient × 10^{-6} (cm^2/s)	
			Human skin *in vitro*			
G	92.1	1410[158]	1.472	66.0 ± 8.0	n/a	159
MPD	90.12	168	1.44	58.0 ± 2.0	n/a	
1,3-BD	90.12	104	1.44	58.0 ± 13.0	n/a	
1,4-BD	90.12	84.9	1.44	65.0 ± 5.5	n/a	
EG	62.07	20.9	1.4316	50.0 ± 11.0	n/a	
DMSO	78.13	1.99	1.47	35.0 ± 9.0	n/a	
			Rat skin *ex vivo*			
G	92.1	1410	1.472	37.7 ± 12.9	3.23 ± 2.21	156
G85		109[158]	1.452	24.6 ± 5.2	1.81 ± 1.13	
G70		22.5[158]	1.428	29.0 ± 10.0	0.86 ± 0.73	
G60		10.8[158]	1.415	33.5 ± 11.6	1.098 ± 0.62	
G50		6[158]	1.399	22.0 ± 7.0	1.04 ± 0.52	
G30		2.5[158]	1.378	8.0 ± 5.0	2.79 ± 1.12	
PG	76.09	42[160]	1.432	50.4 ± 7.8	0.135 ± 0.095	157
PEG-300	285 to 315	~110[153]	1.463	56.7 ± 7.9	1.83 ± 2.22	122
PEG-400	380 to 420	~135[153]	1.465	69.1 ± 4.5, 21.0 ± 6.0	1.70 ± 1.47	122, 161
			Murine skin *ex vivo*			
Gl56	180.16	23.6[162]	1.418	62.0 ± 4.0	1.70 ± 1.47	163
Gl43		6.4[162]	1.398	52.0 ± 9.0	2.70 ± 2.22	
Gl30		2.9[162]	1.379	34.0 ± 7.0	1.40 ± 0.96	
			Rat muscle *ex vivo*			
EG	62.07	20.9	1.428	34.0 ± 0.8	n/a	164
Gl40	180.16	5.5	1.394	16.0 ± 0.6	n/a	
			Porcine myocardium *in vitro*			
Gl40	180.16	5.5	1.391	39.5 ± 3.1	0.48 ± 0.34	165
G58	92.1	8.5	1.414	37.5 ± 0.6	0.77 ± 0.46	
			Human cranial bone *in vitro*			
G	92.1	1410	1.472	16.0 ± 11.0	n/a	166

Table 8 (*Continued*).

OCA	MW (Da)	V (mPa × s)	RI	Efficiency (%)	Diffusion coefficient × 10^{-6} (cm^2/s)	
			Human dura mater *in vitro*			
M16	182.17	≥1	1.357	30.0 ± 1.5	1.31 ± 0.41	167
Gl20	180.16	1.9	1.363	22.0 ± 1.1	1.63 ± 0.29	

5 Optical Clearing for Assessment of Diabetic Tissue Permeability for Chemical Agents

Diabetes mellitus is an endocrine disease characterized by increased glucose level in the body. According to World Health Organization, it is a worldwide growing disease with major cause of heart attack, stroke, blindness, kidney failure, and lower limb amputation.[172–175] These complications are related to the glycation of body proteins which is initiated by a nonenzymatic reaction between the free amino group of the protein molecule and the carbonyl group of the sugar, followed up by cross-linking of proteins[173] and corresponding changes of tissue structure, limitation of its functioning,[174] and cause of metabolic imbalance.[175]

Characterization of tissue permeability for chemical agents allows for assessing the structural changes of tissue,[176] which can be used as a biomarker of tissue protein glycation ability. Degree of tissue glycation measured for noninvasively reachable organs can be used for estimation of tissue condition of unreachable internal organs critical for human life, and thus for monitoring the dangerous complications of diabetes mellitus. Therefore, OCAs may serve as probing molecules for monitoring of tissue structure alterations related to protein glycation.

To prove the concept, kinetics of tissue permeability for selected OCAs can be studied by providing measurements of temporal collimated transmittance for tissue samples from different organs in the process of their OC.[163,177] Such comparative investigations were performed for *ex vivo* skin and myocardium samples of Winstar white outbred male rats using 70% glycerol solution as an OCA and the multichannel fiber-optic spectrometer USB4000-Vis-NIR (Ocean Optics, USA) operating in the spectral range of 500 to 900 nm as a measuring system. Animals were divided into the control and diabetic groups.[177] Diabetic groups included rats with two weeks alloxan diabetes.[175,177–180] Ten skin samples were taken from each group of rats. The mean values of free glucose in blood were measured by glucometer "Accu-Chek Performa" (Roche Diagnostics, Germany) before injection of alloxan, in two weeks after injection; the glucose level was 128 ± 18 and 350 ± 147 mg/dl, respectively.

Obtained results for tissue permeability showed a decrease of myocardium permeability for glycerol from $(11.8 \pm 6.1) \times 10^{-5}$ cm/s to $(8.60 \pm 3.21) \times 10^{-5}$ cm/s in two weeks.[177] In the same time, skin permeability for glycerol decreased from $(1.68 \pm 0.88) \times 10^{-5}$ cm/s to $(1.20 \pm 0.33) \times 10^{-5}$ cm/s in two weeks.[177] Comparing kinetics of collimated transmittance for diabetic and control skin (Fig. 10) and myocardium (Fig. 11) samples, a significantly slower increase of optical transmittance for diabetic samples was found.

The reduction of tissue permeability to glycerol during development of diabetes must be related to alteration of tissue morphology[175] and modification of structure, including the degree of fibril packing, loss of axial packing of the collagen-I fibrils due to the twisting and distortion of the matrix by the glycation adducts,[17,181] the cross-linking of proteins, the change of free and bound water content in tissues, and increase of sarcoplasm viscosity.[174,175,179,182] These structural modifications also lead to the changes of tissue optical properties, specifically to the increase of scattered light intensity.[181]

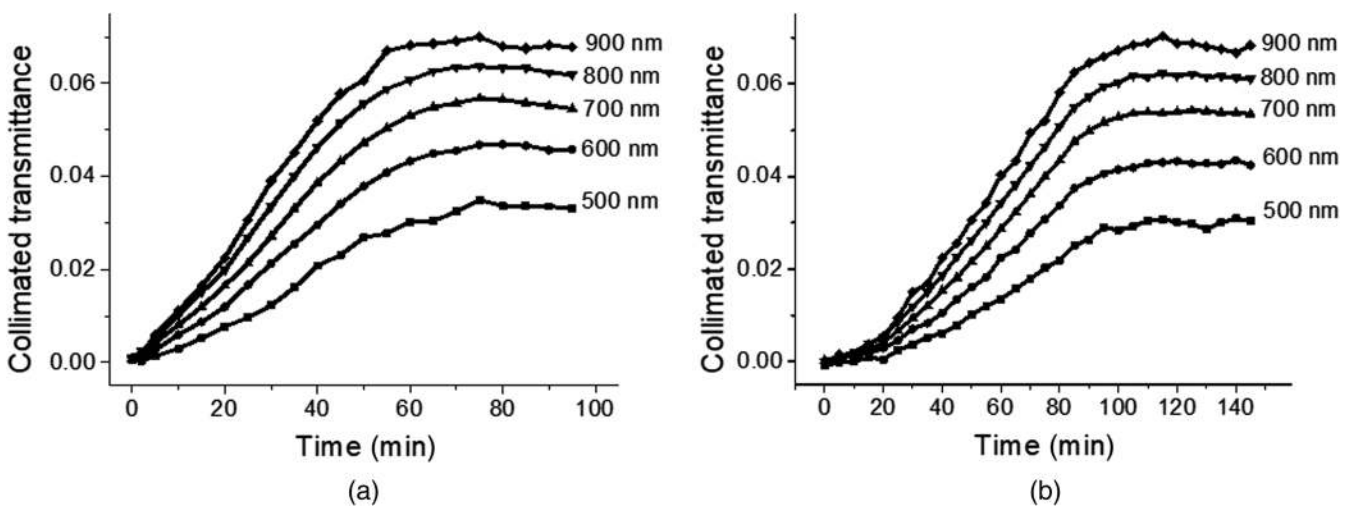

Fig. 10 Typical kinetics of collimated transmittance of the rat skin samples from (a) control and (b) diabetic groups during the OC by 70% glycerol solution.[177]

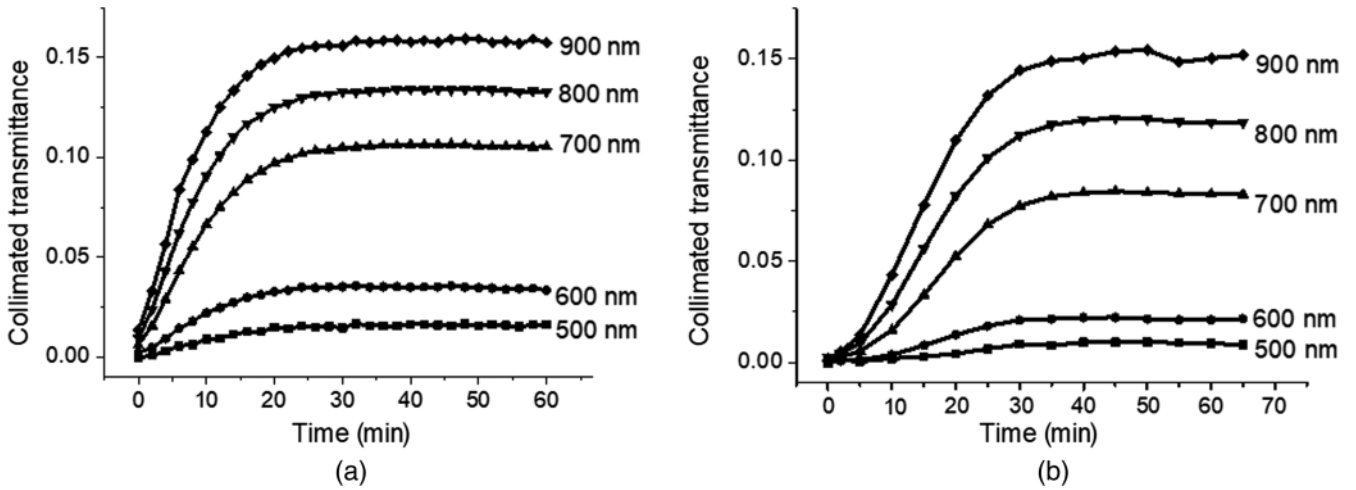

Fig. 11 Typical kinetics of collimated transmittance of the rat myocardium sample from (a) control and (b) diabetic groups during the OC by 70% glycerol solution.[177]

In Ref. 163, up to 2.5-fold slower glucose diffusion in *ex vivo* skin of two-week alloxan diabetes mice was obtained by measuring the collimated transmittance of visible and NIR light through skin samples immersed in 30%, 43%, and 56% glucose solutions.

Presented results show the possibility to develop a method for early diagnostics of diabetes mellitus complications, in particular, for prediction of myocardium damage by detection of skin glycation status. Also, received data for OC of skin and myocardium can be applied in phototherapy, optical diagnostics, or laser surgery to increase light penetration into tissue for diabetic or aged patients.

6 Optical Clearing for Assessment of Blood Microcirculation

The immersion tissue OC method is usually associated with impact on static scatterers, for which scattering ability is under control allowing for reduction of scattering and improvement of applicability of the optical imaging technologies. Apart from the fact that OC decreases light scattering, the penetration (diffusion) of an OCA into the tissue may affect blood microcirculation. In Ref. 183, OC of rat skin at intradermal injection of glucose and glycerol solutions was demonstrated. The decrease of reflectance at injection of glucose was stronger than at glycerol injection but was conserved for a shorter period. For hyperosmotic solutions of glucose and glycerol, the OC of skin was coupled with stasis and dilation of microvessels in the site of application of the agent. As the introduction of OCAs into a tissue may affect blood microcirculation caused by a transient stasis of the microvessels, it is important to study this phenomenon. One of the prospective methods for the assessment of blood flow alterations is the robust laser speckle contrast imaging (LSCI) technique.[184,185] LSCI is based on the registration of the speckle-modulated images, investigation of the spatial and temporal statistics of the speckle pattern by calculation of the contrast K_k of time-averaged dynamic speckles in dependence on the exposure time[185,186]

$$K_k = \sigma_{Ik}/\overline{I}_k = \frac{\sqrt{(1/MN)\sum_{m=1}^{M}\sum_{n=1}^{N}[I_k(m,n)-\overline{I}_k]^2}}{(1/MN)\sum_{m=1}^{M}\sum_{n=1}^{N}I_k(m,n)}, \quad (5)$$

where k is the number of frames in a sequence of speckle-modulated images, $\overline{I}_k$ and σ_{Ik} are the scattered light intensity averaged over the analyzed frame and the root-mean-square value of the fluctuation component of the pixel's brightness, M and N are the number of pixels in rows and columns of the analyzed area of the frame, respectively; and $I_k(m,n)$ is the brightness of the (m,n) pixel of the k-frame.

For example, Cheng et al.[187] used LSCI to evaluate quantitatively OCA induced changes of blood flow. Zhu et al.[55] applied the LSCI to investigate both the short-term and long-term effects of glycerol and glucose, mixture of PEG-400 and thiazone on blood vessels in different tissues *in vivo*. Mao et al.[188] were studied 30% glycerol solution effect on the dermal blood vessels of the rat skin. The recent studies carried out using LSCI were focused on vascular permeability at application of a specific OCA, i.e., Omnipaque™-300, namely, on the analysis of blood flow in pancreatic vessels.[189] Omnipaque™ is a radiopaque agent for x-ray image contrasting with the active substance iohexol. Its aqueous solutions were also used. The solutions were applied to the tissue site topically using a pipette in a volume of 0.5 ml. The calibration of the LSCI system made it possible to quantify changes of the blood flow. Application of 100% "Omnipaque™-300" demonstrates 65% increase of blood flow as 70% "Omnipaque™-300" gives 50% increase of blood flow in the group of diabetic animals (experiments were conducted 16 days after the injection of alloxan). In both cases to 10'th min, blood flow velocity was completely restored. Blood flow in the control group of healthy animals did not show any noticeable changes. Increased blood flow after application of the OCA could be caused by increased vascular endothelial permeability at diabetes even in early stages of disease.

LSCI was used for imaging of cerebral blood flow in newborn mice brain during topical OCA application in the area of the fontanelle.[190] These results demonstrate the effectiveness of glycerol and Omnipaque solutions as OCAs for the investigation of cerebral blood flow in newborn mice without scalp removal and skull thinning. Figure 12 shows the speckle contrast images of the cerebral blood vessel before and during the action of 60% glycerol solution on the newborn mouse skin surface in the fontanelle area. It can be seen that the quality of vascular imaging has been improved significantly.

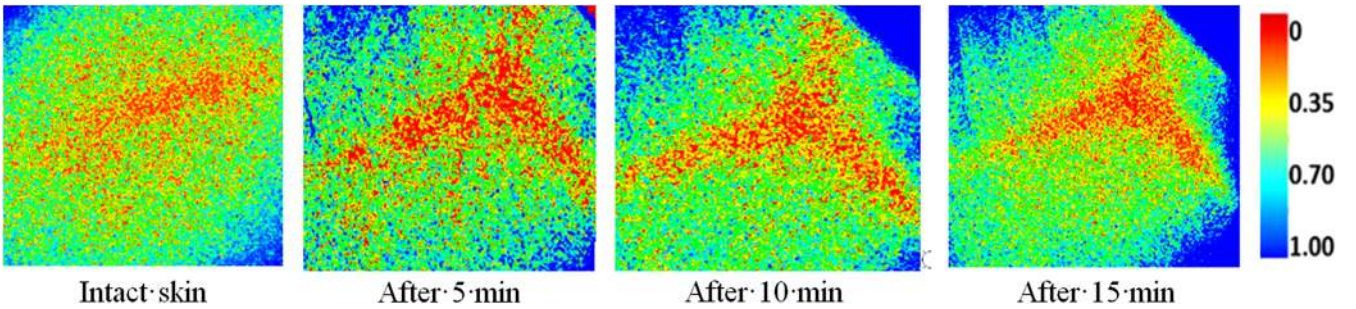

Fig. 12 LSCI of cerebral vessels at application of 60% glycerol solution to skin surface of the newborn mouse in the fontanelle area.

Also it was shown that the Omnipaque/DMSO solution gives better result of OC than aqueous 70% Omnipaque solution. All used OCAs have demonstrated effective skin clearing of newborn mice in the fontanelle area. The OC is more efficient if an aqueous 60% glycerol solution is applied. However, glycerol solution caused a reduction in the cerebral blood flow up to 12%.

7 Optical Clearing of Blood and Enhanced Imaging of Blood Vessels and Cells

The difference of RIs of erythrocytes [red blood cells (RBC)] and blood plasma is the main source of light scattering in blood. There are many OCAs which are used for OC of blood, such as dextrans, iohexol (x-ray contrast, i.e., Omnipaque™), mannitol, glucose, glycerol, PG, PEG, hemoglobin, and some others.[17,53,191–198] The mechanisms of the improvement of light transport in tissue and blood depend on the particular OCA and mode of application.[17,53,161,183,199–211] The RI matching between RBC and blood plasma is one of the major mechanisms of the OC of blood, however, cell aggregation and deformation induced by an OCA or the displacing of blood at OCA flushing may also lead to decreasing of light scattering in blood.[17,53,191–199]

Recently, the experimental studies of the possibility to achieve the fast OC effect in tissues and blood *ex vivo* and *in vivo* using OCT imaging system were performed.[212,213] Several OCAs, such as PEG-300, fructose, and hemoglobin solutions, were used for the enhancement of light transport in the tail veins of mice. The combined application of OCAs for intradermal and intravenous injections in order to obtain rapid OC effect was also studied. A swept source OCT system (Thorlabs, Inc., Newton, Ney Jersey, USA) working at 1300 nm was used. The axial resolution of the OCT system is 12 μm in air (9 μm in water). The OCT system provides a scanning depth range of 3 mm. Measurements were carried out at the tail sites of four mice; the sites of examination were imaged through skin.

The combination of ketamine and xylazine was used for anesthesia or euthanasia of the mice, depending on particular experiment. PEG-300 (Sigma-Aldrich, USA) and hemoglobin solutions (Agat-Med, Russia) with the concentration of 160 g/l were used for intravenous injections into the tail veins of the mice in *in vivo* experiments. In the experiments with euthanized mice, PEG-300 was used for intravenous injections, and dry fructose (Sigma-Aldrich, USA) dissolved in saline with the concentration of 400 g/l was used for intradermal injections. The fructose solution of the volume about 0.05 ml was injected into skin in the projection of the tail vein. The volume of PEG-300 or hemoglobin solution injected into the tail veins was about 0.1 ml, which is about 4% of the total blood volume in a mouse.

The RI of the OCAs used in this study, such as fructose solution, hemoglobin solution, and PEG-300 were 1.4, 1.39 and 1.47, respectively, which are higher than the refractive indices of ISF and blood plasma (1.36 and 1.35, respectively).[17] As it was recently reported, the addition of PEG-300 to blood induced a threefold drop of attenuation coefficient.[212] It was observed that the application of PEG-300 caused a deformation of RBC, their elongation and aggregation. The aggregation of RBC may lead to a decrease of blood scattering caused by "sieve" effect, when a large amount of light travels in blood without interaction with the scatterers.[214] The "sieve" effect has a possibility of exerting some impact on OC in blood.

Figure 13 shows OCT images and corresponding backscattered intensity profiles of the tail vein for two euthanized mice. It can be seen that immediately after injection of PEG-300 the vein walls cannot be recognized [Fig. 13(a)], but in 15 min the vein lumen and tissue structures up and down of the vein can be seen. It is evident that the improvement of light transport is due not only to the less scattering of blood, but also to the penetration of PEG-300 through the vein wall into surrounding tissues during the observation time.

Figures 13(c) and 13(d) show the OCT images of the tail vein area taken immediately and in 15 min after two injections—intravenous of PEG-300 and intradermal of fructose, respectively. The backscattered intensity profiles are also presented. As it can be seen, the tail vein lumen and the reflectance from the tissues lying below the vein can be observed immediately after the intradermal injection of fructose and intravenous injection of PEG-300 [see backscattered intensity profile for Fig. 13(c)], while the injection of PEG-300 into the vein only did not cause the immediate improvement of light transport [Fig. 13(a)]. Fructose solution injected into skin causes local dehydration, partial replacement of ICF by fructose and matching of RIs of skin collagen and ICF that is modified by injected fructose for which RI of 1.47 is exactly equal to RI of hydrated collagen.[17] The collagen reversible solubility in a highly concentrated fructose solution[215] can also decrease light scattering in skin dermis to some later time.

The OCT images of mice tail vein site for *in vivo* measurements, which were performed for two living mice after injection of hemoglobin solution or PEG-300 into the tail vein, are presented in Fig. 14.

The OCT images were captured before and immediately after the injection of hemoglobin or PEG-300 into the tail vein of mice. Because of mouse movements, the OCT images of the same site of the tail vein before and after injection of an

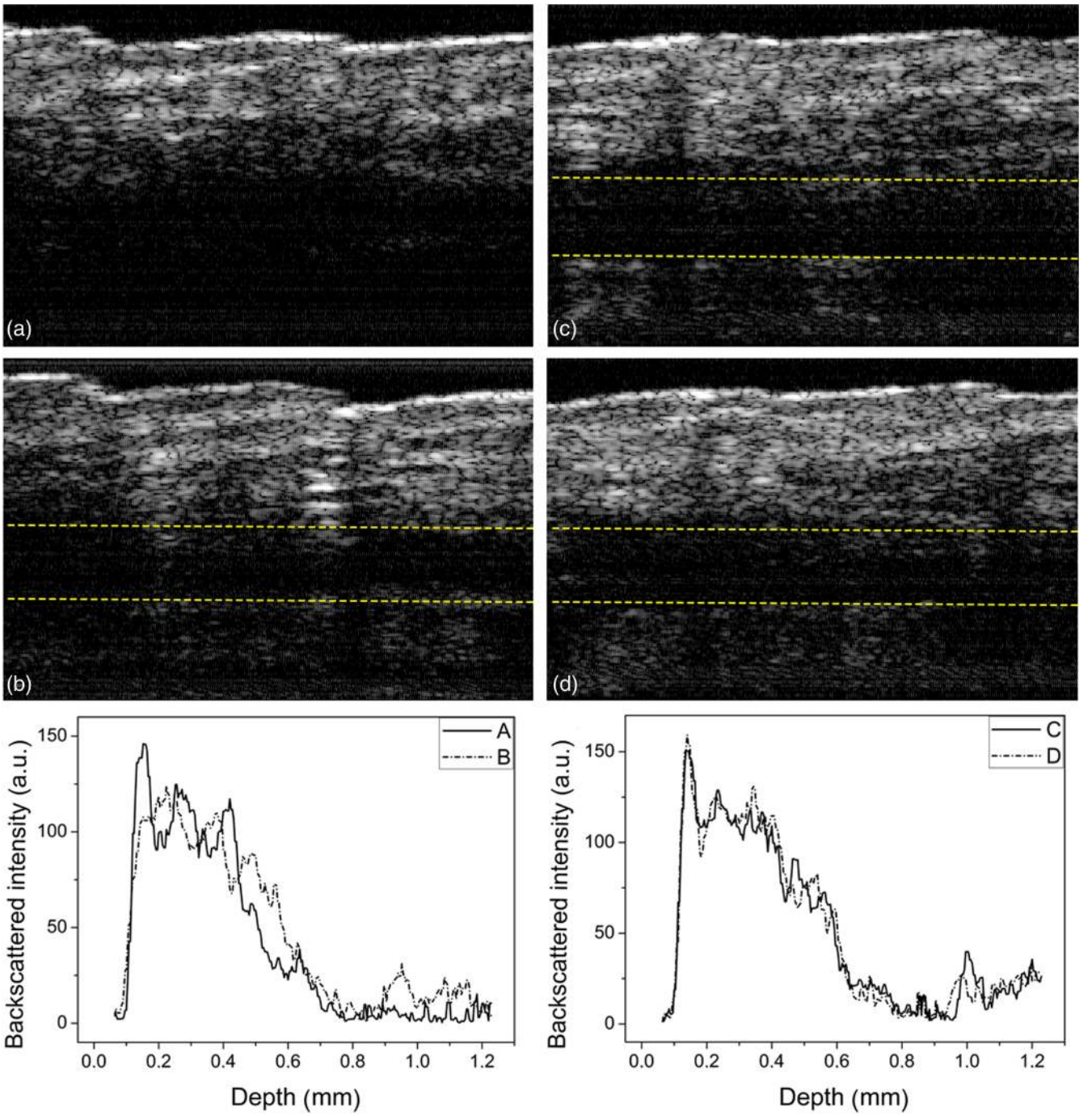

Fig. 13 *Ex vivo* measurements, OCT images (1 × 1.3 mm) and corresponding backscattered intensity profiles of the tail vein for two euthanized mice:[213] (1) (a) taken immediately and (b) in 15 min after injection of PEG-300 into the mouse tail vein and (2) (c) taken immediately and (d) in 15 min after intravenous injection of PEG-300 and intradermal injection of fructose. The yellow dashed lines indicate the approximate position of the vein lumen.

OCA cannot be provided exactly. The sample OCT images as references of the tail vein site before injection of OCAs are shown in Figs. 14(a) and 14(c). Figures 14(b) and 14(d) show the tail vein sites of mice after the injection of hemoglobin solution and PEG-300, respectively. Immediately after injection, a rapid OC was seen for both OCAs: the vein lumen and the tissues above and below the vein can be observed.

As it was discussed for *ex vivo* studies, there are two possible mechanisms of OC of blood: RI matching between RBCs and blood plasma and RBC aggregation. The formation of RBC aggregates enhances the "sieve" effect. Since RBCs are able to disaggregate in the flowing blood due to shear stress, the effect of aggregation caused by an OCA is expected to be reversible.

High RI of free hemoglobin allows one to achieve the RI matching between RBCs and blood plasma and eliminate scattering in blood. In this case, the local hemolysis at the area of interest and consequent release of hemoglobin from RBCs to

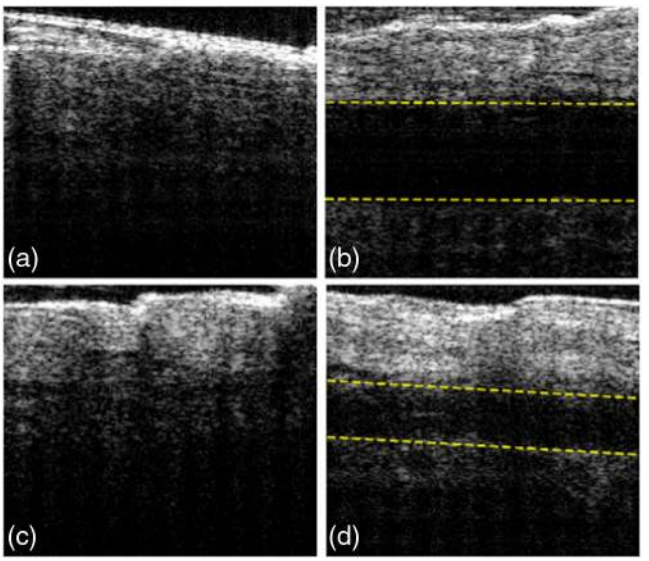

Fig. 14 *In vivo* OCT images (1 × 2 mm) of the tail vein of two living mice: (a) before and (b) after intravenous injection of hemoglobin solution; (c) before and (d) after the intravenous injection of PEG-300.[213] The yellow dashed lines indicate the approximate position of the vein lumen.

plasma can be potentially used for OC of blood layer as it was theoretically[194] and experimentally proved.[216] The use of OCT technique for intravascular imaging requires the insertion of a catheter into the vessel of interest and flushing OCA,[197,198] thus these two technologies can be complementary. However, instead of OCA flushing, hemoglobin as an endogenous OCA can be produced locally in the area of imaging.

It was demonstrated that the combination of intradermal and intravenous injections of OCAs can be used to achieve a rapid OC and increase the probing depth significantly in a short time. Apart from PEG, fructose and hemoglobin solutions, there are many other agents that can be used as OCAs for intravenous and intradermal injections. *In vivo* study demonstrated that combined OC of tissue and blood has a potential to increase the probing depth of OCT not only in endoscopic mode, but also through skin.

Study of microvascular system functioning at the action of OCAs with different osmotic and permeability properties through skin and other biological membranes (barriers)[217–219] is of great importance for understanding of OC mechanisms, tissue and cells physiological reaction[161,183,200–210] and for innovative applications in addition to better tissue transparency.[161,200–211] For example, the combination of increased depth of light penetration and the temporary slowing or even cessation of blood flow in vessels considerably reduces the required radiant exposures for vessel laser photocoagulation.[200,201] Recently, the OC method was demonstrated as an efficient and nondestructive tool of studying blood clot structure and mechanisms controlling clot morphology.[211] The method allows for confocal imaging as deep as 1 mm inside the clot to reconstruct a three-dimensional (3-D) structure of large whole blood clots.

Another coherent-domain optical imaging technique, i.e., LSCI described in Sec. 6, is also beneficial when applied in combination with the OC in order to provide imaging and quantified information about blood flow and vessel diameters in different physiological conditions and drug delivery.[161,202–206] Figure 15 shows typical speckle contrast images of arteries and veins in mouse skin under the conditions of OC by a mixture (9:1) of PEG-400 and thiazone, as well as the behavior of vessel diameters and blood velocity at drug delivery.[206] Noradrenaline (NA) as a common drug for vascular reactivity test was used for intravenous injection.

Various temporal and switchable optical clearing windows (OCWs) to study in depth morphological, physiological, and immunological processes through skin and skull were suggested based on the appropriate combination of OCAs and chemical enhancers of OCA permeability.[161,183,202–210] A skull OCW in combination with two-photon microscopy was recently introduced for repeatedly imaging of neurons, microglia, and microvasculature of mice.[203] The intact skull was topically treated with 10% collagenase or 10% EDTA disodium for 5 to 10 min, and then, with 80% glycerol.

As it was also demonstrated, the mouse footpad, due to its hairlessness, provides an excellent switchable OCW for imaging vascular and cellular structures and function *in vivo*.[207,208] OCW is not only suitable to monitor the cutaneous blood vessels and blood flow distribution by LSCI (see Fig. 15), but also allows for enhanced fluorescent cell imaging using laser scanning confocal microscopy. Therefore, this switchable multiple use OCW gives a possibility of studying blood flow dynamics and cellular immune function *in vivo* for some long period of time of development of vascular and immunological disorders, including disorders induced by such chronic metabolic disease as diabetes.[207,208]

8 Polarization Methods

An analysis of data on the interaction of polarized light with biological tissue can provide a lot of useful information on the structure and status of the tissue. For this reason, polarimetric methods are finding ever increasing use in biophotonics and medicine.[132,133,135–137,220–230] In view of a nonlocal nature of the measured polarimetric quantities and their strong dependence on the measurement conditions as well as because of the optical anisotropy of tissues, each new potential application of polarimetry raises the questions of how to perform the optical experiment to ensure the reproducibility of measurements and the comparability of experimental data, of how to compactly represent the experimental data to minimize the storage requirements, of how to choose basic metrics for tissue characterizations, and of how to retrieve information on a particular component of the tissue from the experimental data. Good answers to the first three questions can often be found using the method of polarimetric rotational invariants proposed and developed in Refs. 231–234. The principal feature of this method is that it deals mainly with polarimetric characteristics that are invariant with respect to arbitrary azimuthal rotations of the sample, uses a broad set of such characteristics, and does not resort to Mueller matrix decomposition.[133] Examples of the use of this method in polarization spectroscopy and polarized light microscopy of tissues are given in Refs. 231–233 and 235. Similar approaches are used in Refs. 236–240.

For the past five years, efforts have been focused on developing effective techniques for characterization of the architecture of collagen-rich tissues, such as dermis, sclera, tendon, and cartilage, at the macroscale[241] and on the assessment of the feasibility of the polarimetric monitoring of glucose content in such tissues.[242] Knowledge of the collagen fiber orientation and ordering is required in studying biomechanics of connective tissues and diseases associated with the abnormalities of such

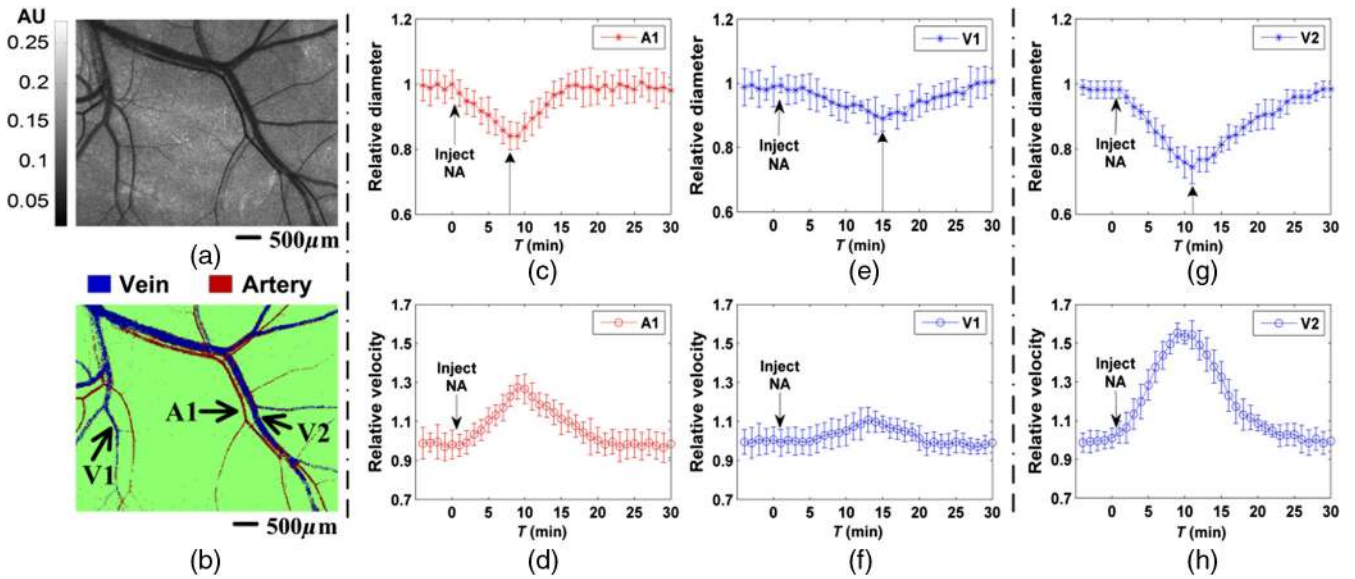

Fig. 15 LSCI under the conditions of mouse skin OC by a mixture (9:1) of PEG-400 and thiazone:[206] (a) speckle contrast image, (b) arteries-veins separation image, NA injection-induced relative changes in vascular diameter and flow velocity in (c) and (d) artery A1, (e) and (f) vein V1, and (g) and (h) vein V2 accompanied by OCA-treatment. The injection time is set to be 0, which is consistent with the arrow shown in (c)–(h). Bar = 500 μm.

tissues.[239,240,243–247] Among the methods being used for characterization of the structure of collagenous tissues at meso- and macroscales are x-ray scattering techniques,[243] multiphoton microscopy,[243–245] light scattering techniques,[244] polarization-sensitive OCT,[246,247] and transmission polarized-light microscopy mapping (TPLMM).[239,240,245] The advantage of TPLMM is the ability to have a wide field of view in combination with good resolution. In Refs. 241 and 248, it has been shown that TPLMM can be employed for characterization of collagenous structure in thick (up to 2 mm) tissue samples with the use of immersion OC. This makes the technique even more appealing, since it obviates the need for histological sectioning of tissue. As an illustration, Fig. 16 shows TPLMM maps for a nonsectioned rabbit sclera specimen, a tissue stripe extending from the cornea to the optic nerve. The sample was incubated in 85 vol% aqueous glycerol solution for 3 days. The average thickness of the sample was 790 μm. The measurements were performed using a microscopic polarization mapping system described in Ref. 241. This figure shows the maps of three characteristic angles: the phase retardation angle Δ_r, the angle of optical chirality ϕ, and the polarization mid-axis orientation angle υ.[241] These angles are defined by the relations

$$\cos 4\upsilon = \tilde{B}_2/\sqrt{\tilde{B}_2^2+\tilde{B}_4^2}, \quad \sin 4\upsilon = \tilde{B}_4/\sqrt{\tilde{B}_2^2+\tilde{B}_4^2},$$

$$\cos 2\varphi = \tilde{B}_1/\sqrt{\tilde{B}_1^2+\tilde{B}_3^2}, \quad \sin 2\varphi = -\tilde{B}_3/\sqrt{\tilde{B}_1^2+\tilde{B}_3^2},$$

$$\Delta_r = 2\arccos\sqrt{\sqrt{\tilde{B}_1^2+\tilde{B}_3^2}/\left(\sqrt{\tilde{B}_1^2+\tilde{B}_3^2}+\sqrt{\tilde{B}_2^2+\tilde{B}_4^2}\right)},$$

where

$$\tilde{B}_1=(m_{22}+m_{33})/4,\ \tilde{B}_2=(m_{22}-m_{33})/4,$$
$$\tilde{B}_3=(m_{23}-m_{32})/4,\ \tilde{B}_4=(m_{23}+m_{32})/4,$$

m_{ij} being the elements of the Mueller matrix of local transmission of the sample. In this example, the angle υ bears information on the average preferred direction of orientation of collagen fibers. The angle ϕ depends on the azimuthal variations of the local optic axis (the preferred collagen fiber direction) across the layer thickness. In the absence of such variations, $\phi = 0$. The retardation Δ_r depends on the orientational order of collagen fibers and thickness of the sample in the probed region.[241]

Figure 17 shows another example of the use of our TPLMM technique. Here this technique is employed for characterization of the structure and optical properties of RTT fascicles. Figures 17(a) and 17(b) show maps of the characteristic angles υ and ϕ for an unloaded RTT fascicle sample. The υ map reveals a waviness of the collagen fibers (crimp),[140] and the ϕ map shows significant variations of the preferred collagen fiber direction across the thickness. For comparison, mapping results for a slightly stretched tendon fascicle sample are shown in Figs. 17(b) and 17(c). In contrast to the unloaded sample, here spatial variations of υ are very slow, as if the collagen fiber orientation throughout the fascicle was uniform. At the same time, the ϕ map shows small but regular variations of the collagen fiber orientation across the thickness. Figures 17(d)–17(h) shows the possibility of estimating spatial and wavelength dependences of the average effective birefringence index $\langle \Delta n_{\text{eff}} \rangle$ of the tissue.

9 Molecular Modeling of Immersion Optical Clearing of Biological Tissues

The immersion OC mechanisms at the molecular level are still not yet clearly understood.[249] Thus molecular level studies in this field are important and could propose molecular agents with a set of beneficial properties. This section presents a short summary of the recent results on molecular modeling of the interaction of some low molecular OCAs with collagen and finding the correlations between the interaction parameters and EOC.[250,251]

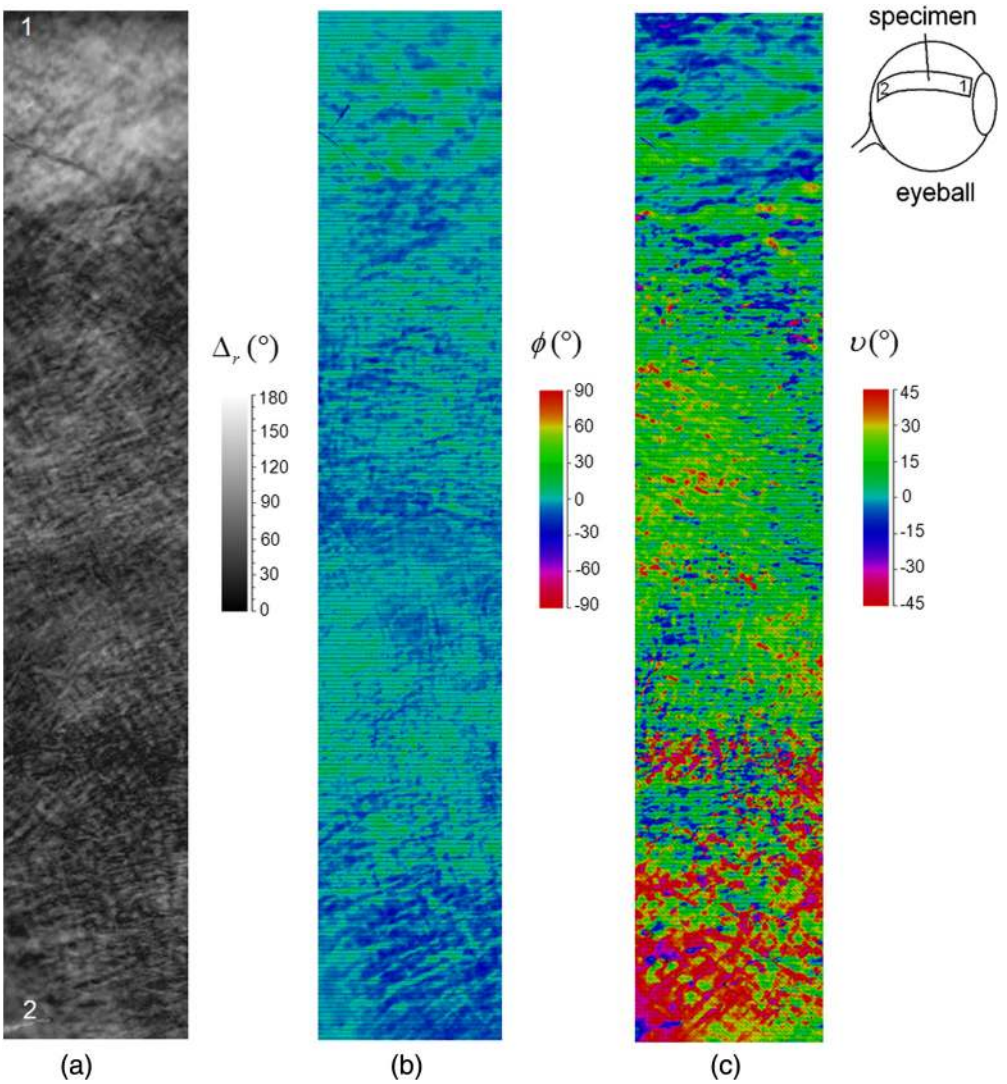

Fig. 16 Mapping results for a rabbit sclera specimen optically cleared in 85 vol% aqueous glycerol solution for 3 days: (a) map of retardation Δ_r, (b) map of ϕ, and (c) map of υ; 1 and 2 mark the anterior and posterior regions, respectively. The mapped area is 1.3 mm × 7.3 mm; $\lambda = 544$ nm.[248]

Following Ref. 249, to characterize EOC, the reduced scattering coefficient ratio (RSR) defined as the ratio of reduced scattering coefficients before and after OCA application to dermal side of skin during 45 min was used. The RSR function on concentration of OCA allows one to define optical clearing potential (OCP) as a slope determined from linear regression analysis of this function for each studied chemical agent.

The interaction of six low-molecular tissue-clearing agents (1,2 and 1,3-propanediol, EG, glycerol, xylitol, and sorbitol) with the collagen mimetic peptide $(GPH)_3$ was studied by applying the methods of classical molecular dynamics and quantum chemistry.[250] The correlations between the OCP and such intermolecular interaction parameters as the amount of time of the agent being in a hydrogen-bonded state with the collagen, the dependence of the volume occupied by the collagen in an aqueous solution on OCA concentration and the probability of a double hydrogen bonds formation between the agents and the collagen were carried out by the methods of classical molecular dynamics in the GROMACS program with the AMBER03 force field. The initial intermolecular complex configurations were obtained in the molecular docking program called AutoDockVina. The optimization of geometry parameters of the complexes and individual components was performed by parameterization method 6, and the interaction energies were calculated by means of a single stem cell factor procedure by B3LYP/6-31G(d) method in the Gaussian program.

The complex molecular modeling analysis showed that for the OCAs under study, the effectiveness of interaction with the collagen depends both on the number of alcohol groups and the distance between them (Fig. 18). Moreover, the conformational mobility of the low molecular agents should be taken into consideration. The higher this mobility is, the better an agent can adapt to the molecular pocket. There are four groups available for the classical hydrogen bonding formation in the site pocket of a collagen model under study: two carbonyl (one at a glycine residue, the other at a hydroxyproline residue of the same α-chain) and two alcohol ones at hydroxyproline residues of different α-chains. The 1,2-propanediol molecule has the shortest distance between the alcohol groups of all the diatomic alcohols in question, thus, it forms two hydrogen bonds only with the oxygen atoms of the carbonyl groups ($\Delta E = 23$ kJ/mol). The length of sorbitol, hexatomic alcohol,

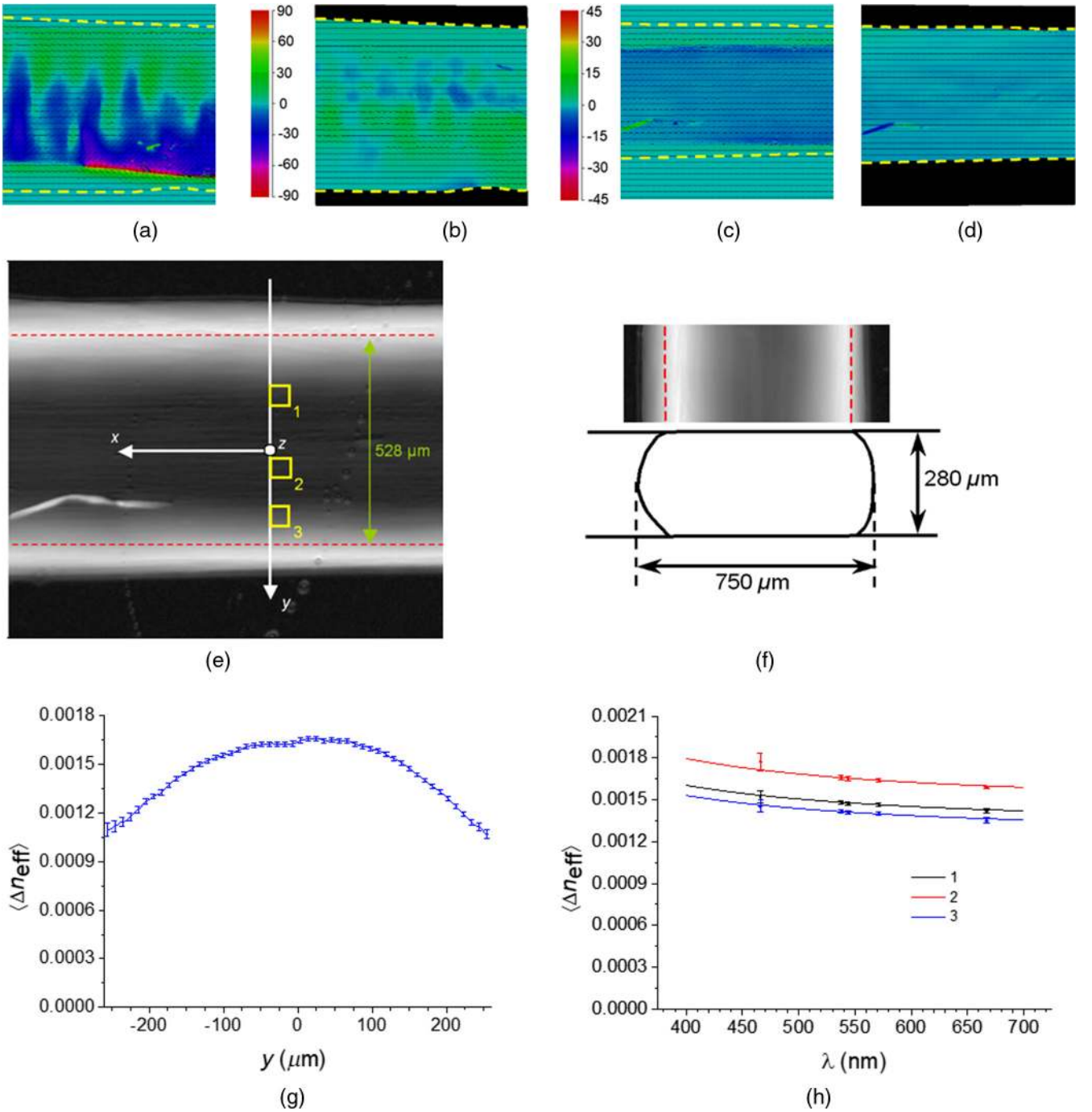

Fig. 17 Results for an RTT fascicle imbibed with glycerol and placed in glycerol between an object-plate and a cover-slip:[241] the fascicle is not loaded, maps of (a) ϕ and (b) υ; (c) and (d) same as in (a) and (b), but the fascicle is slightly stretched: maps of (c) ϕ and (d) υ. The maps shown in (a)–(d) were measured at the wavelength $\lambda = 544$ nm. (e) Map of Δ_r for the loaded fascicle at $\lambda = 466$ nm and the reference system used. The width of the mapped area in (a)–(e) is 1.12 mm. (f) The cross section of the loaded fascicle reconstructed from its OCT-image and a fragment of the map of Δ_r at $\lambda = 544$ nm. Red dotted line shows boundaries of the area within which the tissue is in contact with the object-plate and the cover-slip (in this region, the thickness of the specimen varies in the range 270 to 280 μm due to a tilt of the cover-slip). The approximate position of the scan section corresponds to the *y*–z plane in (e). The average effective birefringence index of the loaded sample at $\lambda = 544$ nm as a function of position along the *y*-axis. (g) The average effective birefringence index for each value of *y* was obtained by averaging over the interval, 100 μm < *x* < 0. (h) Wavelength dependences of the average effective birefringence index for three regions of the loaded fascicle. Adapted from Ref. 241.

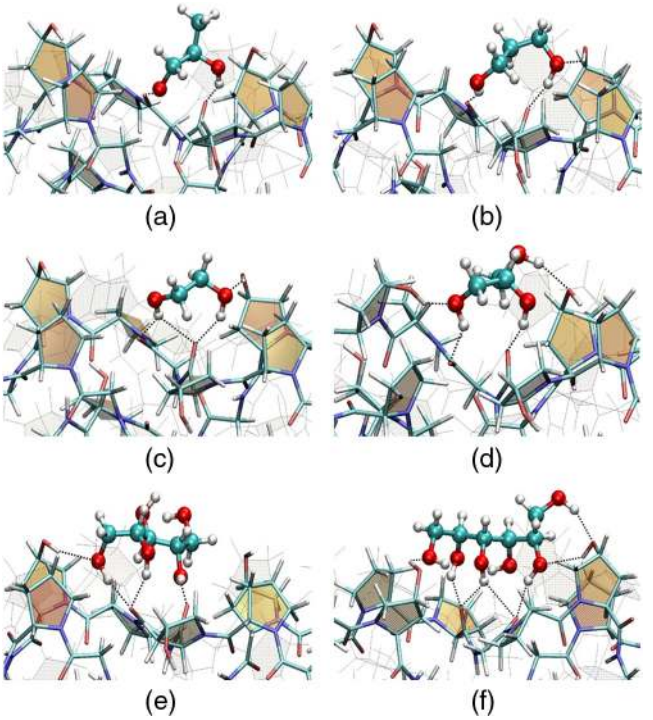

Fig. 18 Structure of hydrogen binding complexes formed between collagen units $[(GPH)_3]_2$ and OCAs: (a) 1,2-propanediol, (b) 1,3-propanediol, (c) EG, (d) glycerol, (e) xylitol, and (f) sorbitol. Classical intermolecular hydrogen bonds are shown with dashed lines. Adapted from Ref. 250.

is enough to form six effective hydrogen bonds, which significantly influences the interaction energy ($\Delta E = 80$ kJ/mol).

Figure 19 shows the dependence of the OCP of rat skin[249] on the interaction energy of the collagen peptide molecule with the molecule of the OCA (a) and the number of hydrogen bonds between them per unit time (b) for various types of OCAs.[250] It is clearly seen that they correlate well with each other. The calculated correlation coefficient is of 0.94 and 0.76 for the interaction energy and the number of hydrogen bonds between them per unit time, respectively. The energy of intermolecular interaction of dextrose molecule with the chosen collagen model that turned out to be 94.5 kJ/mol was additionally calculated to check predictive options of the correlation. The predictive value of the dextrose OCP for rat skin was 0.383 and it falls into line with experimental data, which is 0.387.[249]

Such high correlation coefficients make it possible to state a key importance of the postdiffusion stage of OC where the interaction of collagen and OCAs, and its impact on tissue OC is significant. The results of the study allow one to state that in the course of interaction there is a partial substitution of water molecules that are connected with collagen by molecules of the OCA. It leads to the disturbance of the hydrogen bond net and to reversible dissolving of collagen fibrils. In its turn, their refraction index decreases and they are adjusting to the intrafibrillar medium. The greater affinity to collagen, which is characterized by the intermolecular interaction energy, an OCA has, the more effective is the process.

Another informative parameter to characterize correlation between OCAs interacting with collagen and OCP is the protein volume change. Currently, a lot of experimental data assessing tissue EOC with glycerol and other OCAs are available.[17,156,252] It is worth mentioning that different authors use different parameters to assess EOC. For instance, Genin et al.[156] use collimated light transmission coefficient, whereas in Ref. 252 the volume of light that enters into tissue and the light penetration depth measured by OCT.

Within the framework of molecular modeling[250] has been the relation between collagen peptides volume change and glycerol concentration (Fig. 20). This figure shows that this relation is nonlinear: its maximum is reached at medium-range glycerol concentration (40%). Experimental data analysis of human skin OC by means of glycerol[156,252] shows that the EOC is at its maximum at higher concentration (60% to 70%). This difference can be explained in the following way: when this interaction is molecularly modulated, the glycerol concentration is

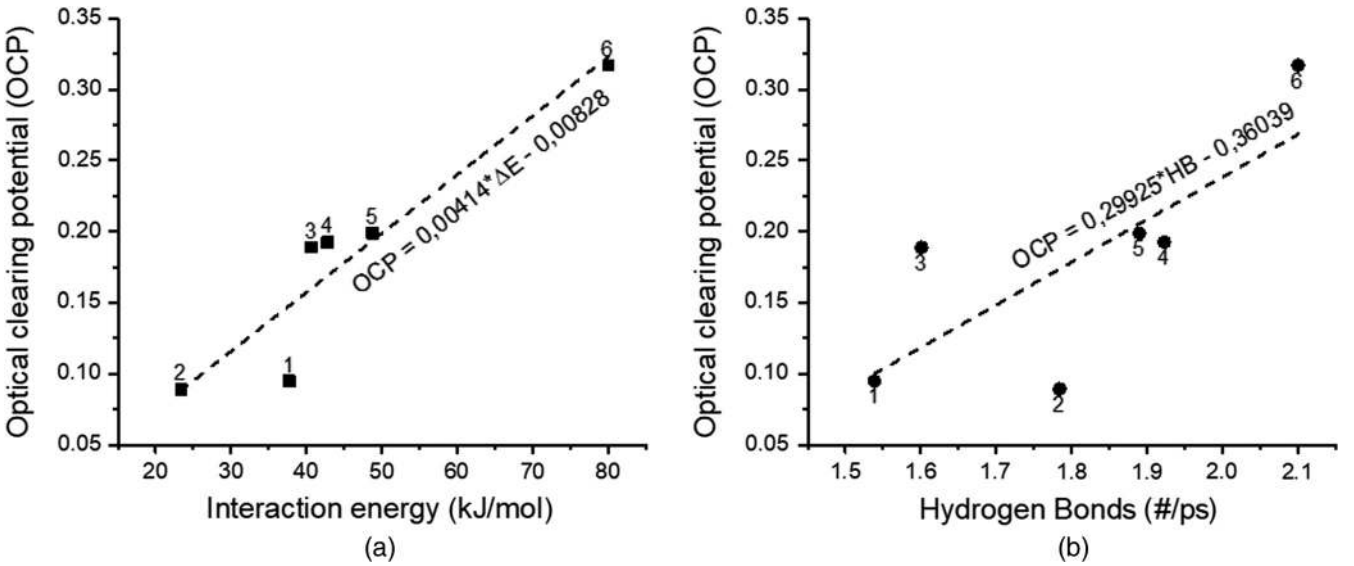

Fig. 19 (a) Dependence of the OCP of rat skin and human skin[249] on the interaction energy of the collagen peptide molecule with the molecule of the OCA and (b) the number of hydrogen bonds between them per unit time for various types of OCAs. Numbers indicate types of OCAs: (1) EG, (2) 1,2-propanediol, (3) 1,3-propanediol, (4) glycerol, (5) xylitol, and (6) sorbitol.

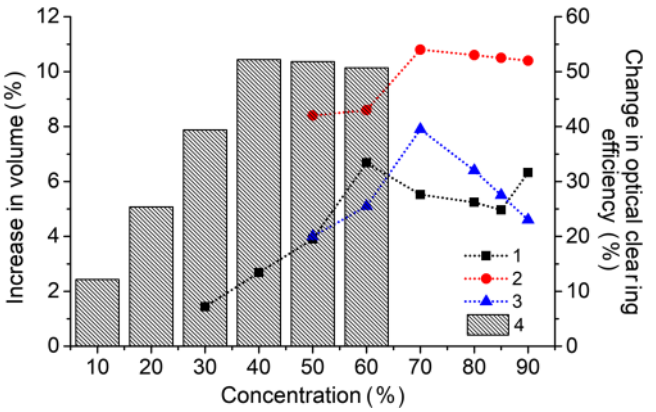

Fig. 20 Experimental data for EOC dependence on glycerol concentration: 1 is the coefficient of collimated transmission,[156] 2 and 3 are the volume of light that enters into tissue and the light penetration depth measured by OCT,[252] and 4 is the dependence of collagen peptide volume change on glycerol concentration.[250]

set inside the intercellular space, while the experimental data indicate glycerol concentration prior to skin application. Since the tissue already has some amount of liquid inside, it can be expected that the glycerol concentration inside the tissue will be smaller than an applied one.

The influence of concentration of the other OCAs on the collagen molecule volume is presented in Fig. 21. It reveals that the dependence of volume of the collagen peptide molecule is nonlinear. Almost all agents have a maximal impact on the volume of collagen fibers in the range of medium concentrations.

Maximum of collagen molecule volume achieved at medium-range glycerol concentration can be explained in the following way. First, collagen surface has a finite number of seats, i.e., "molecular pockets" suitable for efficient attachment of glycerol molecules. Second, the molecular modeling reveals that the higher the concentration of glycerol is the more probable is the formation of hydrogen-bound self-associates. With time these self-associates form cluster structures, which leads to nonuniform impact on different areas of collagen molecules. In its turn, this decreases the destruction rate of collagen hydration shell and, subsequently, decreases glycerol influence on collagen.

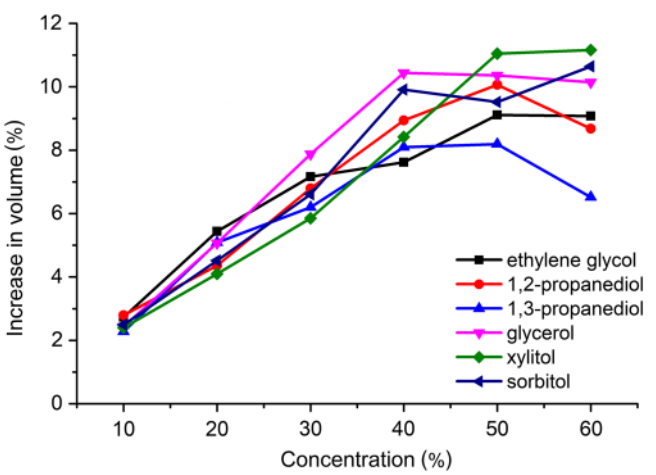

Fig. 21 Dependence of volume of collagen peptide molecule in water solution on concentration of different OCAs.[250]

Based on the performed molecular modeling, the mechanism of collagen fiber swelling under glycerol impact can be described as follows: when attached, glycerol molecules of the greatest affinity to collagen push out the water bound to it. This disrupts the net of hydrogen bonds between collagen fibrils and leads to fibril protein swelling. The disruption of hydrogen bonds net occurs because glycerol molecules bound to collagen by alcohol groups, "stick out" their hydrophobic parts (CH_2-groups), and prevent formation of new hydrogen bonds.

10 Adipose Tissue Optical Clearing by Heating and Photodynamic Treatment

Adipocytes constitute the main cellular component of AT and are the major storage depots of the energy in the form of triglyceride (TG) droplets. Absorption of the human AT is due to absorption of hemoglobin, lipids, and water (~8% to 11%);[17] its scattering is a very complex phenomenon and strongly depends on the temperature.[253–256] The OCT studies demonstrate well reduction of light scattering on the cellular level due to the phase transition of TG localized in cell lipid droplets from crystalline to liquid phase for the temperatures from above 35°C.[256]

Recently, it was shown that photodynamic/photothermal effects induced in AT stained with brilliant green or indocyanine green (ICG) under irradiation at 442/597 nm or 808 nm, respectively, lead to lipolysis of fat cells.[257,258] Fat cell lipolysis can also be induced in the course of LLLT.[259,260] The final products of cell lipolysis contribute to OC of the cell layers over entire body sites, where the cells are expressed for lipolysis. Local fat cell lipolysis is the breakdown of lipids and involves hydrolysis of TGs into glycerol, which works as an OCA, and FFAs, which are good enhancers of tissue permeability.[54–56,120,159,259–265]

It was proved that due to light-induced cell membrane porosity, the intracellular content of the cell percolates through the arising temporal pores into the interstitial space.[266] As a consequence, the RI of the ISF (initially equal to $n_i \cong 1.36$)[267] becomes closer to the RI of the matter inside the adipocytes, mostly lipids of a lipid droplet (RI of lipids, $n_a \cong 1.44$).[53] Due to the RI matching, the tissue sample becomes optically more homogeneous and more transparent to light.[253,255,266–268]

Figure 22 shows a series of two-dimensional (2-D)[269] and 3-D images illustrating the alteration of optical properties of ICG-sensitized and then laser irradiated [underwent photodynamic treatment (PDT)] AT sample that was kept at the temperature of 41°C during a prolonged observation. It can be seen that: (i) brightness (optical transmittance) variations are predominantly characteristic to the intercellular space and (ii) optical transmittance becomes homogeneous over the image area with a long-time elapsed after 1-min laser exposure. The spatial resolution of the measuring system was about 1 pixel/μm. Encoding the state of one pixel by one byte, one may get 256 different shades of gray for evaluation of the local brightness of transmitted light.

The phenomenon observed may take place due to increased permeability of adipose cell membranes in ~10 min after laser irradiation. Therefore, the extracellular space is filled up by the products of cell lipolysis, which leads to RI matching between cells and interstitial space; this process takes about 9 min (from the 10'th to the 20'th min; see Fig. 22). As a result, tissue becomes optically more homogeneous, what can be easily seen in the images of Fig. 22. It is interesting to note that in

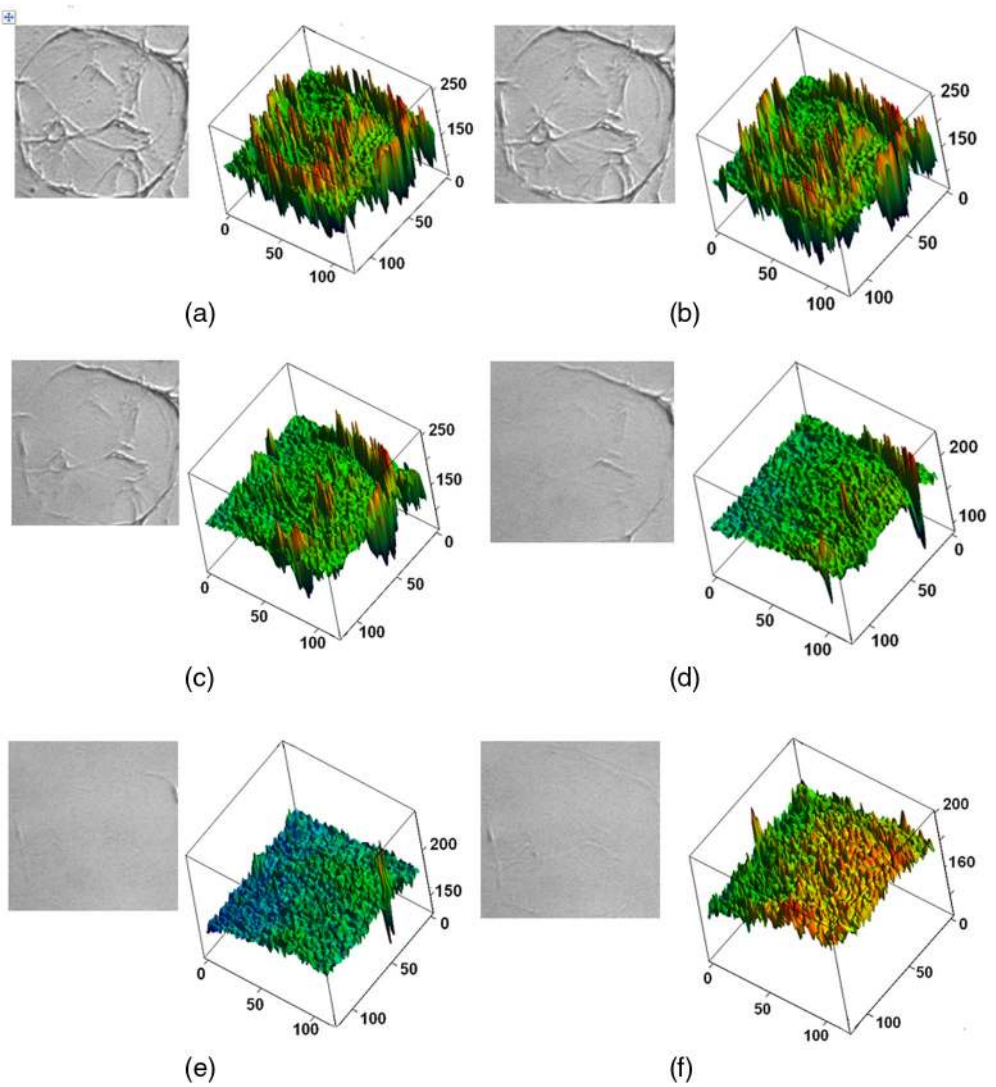

Fig. 22 PDT action for ICG-sensitized and laser irradiated sample of subcutaneous human fat tissue: 2-D microscopic white light images (left upper corner) of the selected adipocyte area[269] and corresponding 3-D representation of brightness images for transmitted light through 150-μm-thick sample, (a) before and (b)–(f) after 1-min irradiation by a continuous wave (CW) diode laser (808 nm) with the power density of 250 mW/cm^2. The time interval between the image recording and the end of light exposure is (b) 10 min, (c) 16 min, (d) 26 min, (e) 30 min, and (f) 37 min. The sample temperature was kept at 41°C.

spite of observed increase of optical homogeneity of tissue sample, the spatially averaged brightness practically did not change in time. Figure 22 shows that for earlier observation time (0 to 16 min), the images show the sharp peaks of brightness, which are mostly characteristic to the cell periphery regions and can be associated with cell refraction and wave guiding properties. At the same time, such localized strong brightness are not observed at later observation time (26 to 37 min), which is the sign of tissue optical homogeneity. This may prove that PDT provides fat cell lipolysis via the increase of cell membrane permeability; intracellular content flows out of cells and fills up the intercellular space mostly by the products of lipolysis, such as glycerol and FFAs; subsequent RI matching of intercellular and intracellular spaces makes brightness more homogeneous within the tissue area underwent PDT.

The OCT images presented in Fig. 23 clearly show temporal changes of fat tissue cell morphology after PDT action at 37°C. The characteristic time for such changes of 120 min correlates well with the expected biological response to PDT.[255] The major changes after irradiation are seen on the upper layer of the cell structure. At physiological temperature of 37°C, ICG-mediated 808-nm diode laser treatment led to the large cell damage depth, equal approximately to 230 μm [Figs. 23(b) and 23(c)]. The average size of adipocytes was 60 to 70 μm (vertical size in optical length units). The arrow in Fig. 23 marks the intensity peak from the lower reflecting sample boundary {i.e., related to optical transmission of the sample [see Fig. 23(d)]}. To illustrate that besides PDT, the thermal treatment also produces lipolysis; in Fig. 23(e), the temperature dependence for light transmittance through a sample of pork fat is presented.[253,254] The total intensity of transmitted white light was calculated as $I = \int_S I(s)\mathrm{d}s$, where S is the surface area of the sample (is equal to the area of the image), $I(s)$ is the intensity of an elementary segment of the image (the pixel intensity), and $\mathrm{d}s$ is the area of a pixel (6.5×10^{-5} mm^2).

The enhanced porosity of adipose cell membrane for ICG-mediated PDT was studied *in vitro*.[269,270] The hypothesis of

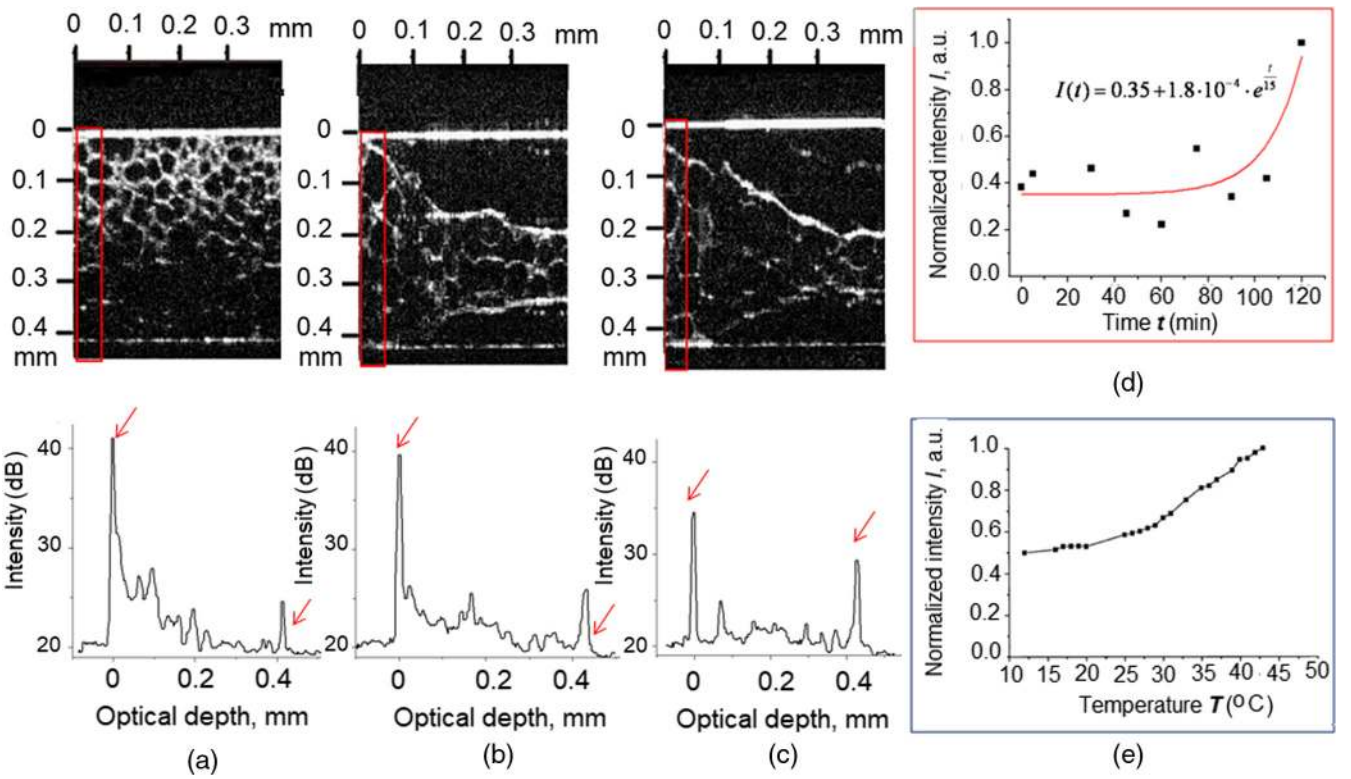

Fig. 23 PDT action for ICG-sensitized and laser irradiated sample of subcutaneous human fat tissue: OCT images of fat tissue sample (a) before and (b) immediately after laser irradiation during 5 min by CW diode laser (VD-VII DPSS, 808 nm, 250 mW/cm^2), and (c) after 120-min of observation. The down curves are the corresponding A-scans averaged over selected B-scan area (between two red vertical lines).[255] The red arrow marks the intensity peak from the bottom reflecting sample boundary (i.e., related to optical transmission of the sample). (d) Temporal dependence of normalized intensity peak from the bottom reflecting sample boundary of A-scans of OCT images (red line is the approximation curve; $R^2 = 0.7$). The concentration of ICG was 1 mg/ml and sample temperature was 37°C.[255] (e) Temperature dependence for light transmittance through a sample of pork fat averaged over the sample area (6.5×10^{-5} mm^2).[253,254]

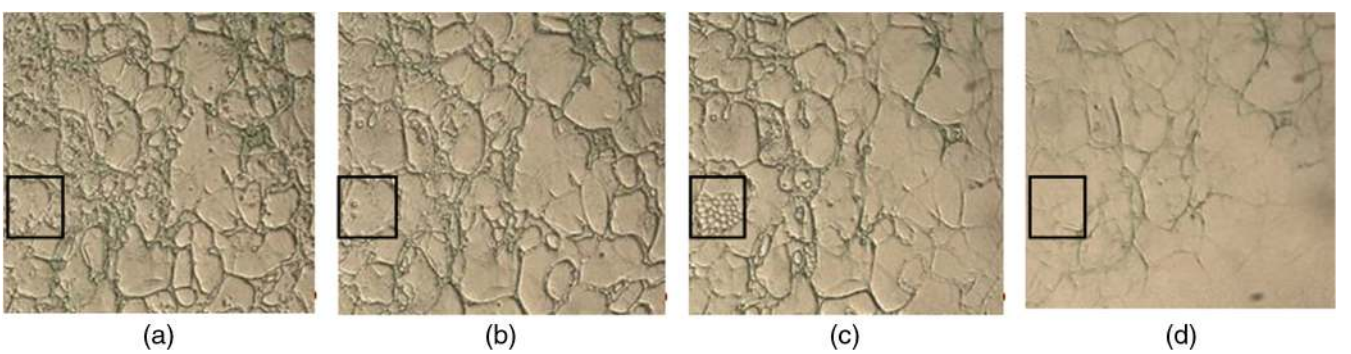

Fig. 24 Transmittance white light images of ICG-stained subcutaneous fat tissue sample (a) before and (b) and (c) after laser irradiation by CW diode laser (808 nm) with the power density of 250 mW/cm^2 during 1 min. The time interval between the image capture and the end of light exposure was (b) 1 min, (c) 13 min, and (d) 127 min. The sample temperature was 33°C.

PDT-induced pore formation is in good agreement with the experimental results.

Figure 24 shows the transmittance white light images of ICG-stained subcutaneous fat tissue sample (a) before and (b)–(e) after 1-min irradiation by CW 808-nm diode laser with the power density of 250 mW/cm^2. The cell lipolysis is seen that stimulates the leakage of a part of intracellular fluid into the intercellular space, thus the tissue gradually undergoes immersion clearing.

According to Fig. 24, at the initial moment, the dye is concentrated in the intercellular space (green color). Then the dye stains the cell membranes. The cell content is gradually released after irradiation (which results in the matching refractive indices of intracellular and intercellular fluids and increase of optical

transparency of the sample). Small lipid vesicles are well seen in the intercellular space (within rectangular area selected in Fig. 24).

Photochemical processes are initiated in the ICG-stained cell as a result of laser irradiation. Unsaturated fatty acids, which constitute 65% to 85% of human fatty tissue, are sensitive to sensitized photooxidation.[271] Moreover, their sensitivity increases in proportion to the number of double bonds in the fatty acid chains.[271] Cholesterol is easily oxidized as well. Malondialdehyde is an important toxic product of peroxidation of unsaturated fatty acids[272,273] and may be involved in prolonged biological response on a rather short (1 min) PDT. There are two major pathways of fat cell permeability control mediated by ICG at laser irradiation: (i) when at the first stage of the photochemical reaction all processes involved are triggered by generation of singlet oxygen and (ii) when (60 min later) the toxic products of ICG decomposition have an effect.[274,275] The change in permeability and stability of the cell membrane occurs in this case due to the structural defects of the membrane bilayer as a result of the membrane lipids oxidation.

11 Wavefront Shaping and Computational Tissue Optical Clearing

In addition to immersion OC, more sophisticated methods based on controlling of the incident light wavefront can be used for the suppression of impact of strong light scattering on focused beam degradation and may improve significantly the image quality in tissue depth.[276–283] Most of these techniques use spatial light modulators to compensate the many spatial degrees of freedom of light at its transport in the scattering medium.[280,281] It was found that at wavefront control the multiply scattered light forms a focus with a brightness that is up to a factor of 1000 higher than the brightness provided at transport of the uncontrolled beam.[280] Reviews of recent progress of focusing, shaping, and compressing waves propagating in strongly scattering media by controlling the many degrees of freedom in the incident waves and advances in application of wavefront shaping (WS) techniques in biomedicine are presented in Refs. 281 and 282.

The simultaneous application of immersion OC and WS seems to be a prospective approach because application of the OCA reduces optical inhomogeneity of a highly scattering tissue, and the WS controls incident light beam to eliminate noncompensated influence of multiple scattering. As a result a sinergy in enhancement of the penetration depth and signal-to-noise ratio is provided. It has been recently demonstrated that WS-OCT applied in combination with 70% glycerol solution as an OCA reveal hidden structures of *ex vivo* mouse ears inaccessible with conventional OCT imaging (see Fig. 25).[283]

It was also shown that computational or analytical OC can be applied as a noninvasive method to evaluate concentration of cutaneous chromophores at deep tissues.[284] The analytical OC uses the ability of diffuse reflection spectroscopy to reconstruct distribution of a particular chromophore of interest, which is normally hidden on the background of absorption of stronger tissue chromophores such as hemoglobin, melanin, and water and strong light scattering. The method has been successfully demonstrated in application to extraction of absorption coefficient of beta carotene inside tissue phantom based on the mouse ear alone and together with immersion and compression OC.[284]

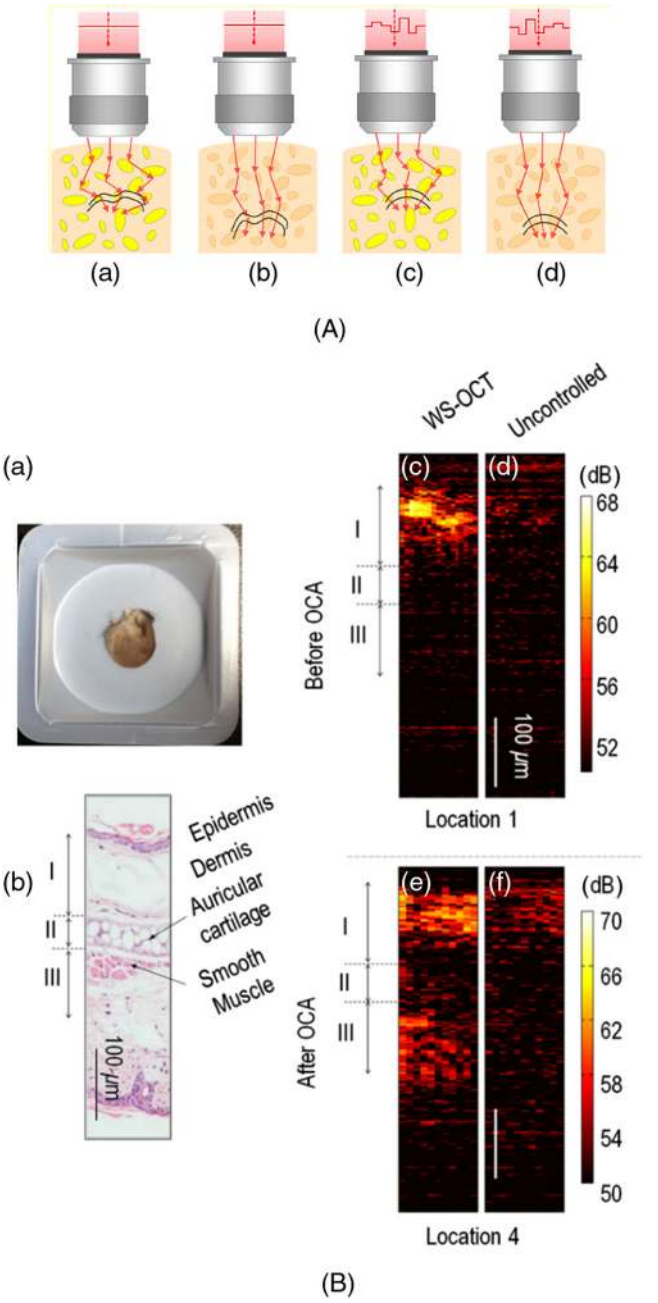

Fig. 25 (A) Principle of combined immersion OC and WS in a OCT system: conventional OCT imaging (a) after the application of an OCA, (b) the overall scattering of the tissue is reduced, (c) WS in OCT, the optimal incident wave-front generates a tight focus inside the tissue, and (d) combined effect of OCAs and WS, maximal penetration depth can be achieved due to reduction of tissue scattering and incident light beam optimal focusing. (B) Tissue sample: (a) dissected mouse ear, (b) histology of the ear, (c) and (d) OCT images acquired before the OCA application, (e) and (f) images acquired after the OCA application (70% glycerol solution for 1 h), (c) and (e) images optimized by WS, and (d) and (f) acquired for uncontrolled beam at locations 1 and 4.[283]

12 Optoacoustic/Photoacoustic Imaging

In the previous sections, it was well demonstrated that OC is a powerful method to modify temporally and reversibly tissue and blood scattering properties for enhancement of the probing depth and image quality of different optical modalities applied

in *in vitro*, *ex vivo*, and *in vivo*. Nevertheless, for the two last decades, it was not evident that OC could help for optoacoustic (OA) [photoacoustic (PA)] imaging techniques based on absorption as an intrinsic contrast and for which the role of scattering is to illuminate absorbing target homogeneously.[1,17] Recent studies from different research groups on immersion OC at application of widely used OCAs to OA/PA systems showed great benefits expressed in much better probing depth and spatial resolution of these systems.[198,285,286–293] First, it was demonstrated for optical resolution PA microscopy (OR-PAM) in two different modifications.[287,288] As in OR-PAM, the lateral resolution is determined by the diffraction-limited light focusing, which degrades due to light scattering, and the probing depth is limited by the photon transport mean free path, which is also in tissues determined by light scattering, suppression of scattering at tissue interaction with an OCA strongly improves these characteristics of the microscope.[287] As an OCA, authors used a 88% glycerol–water solution. To avoid slow transepidermal diffusion of the OCA in *in vivo* studies, they directly injected solution into the mouse scalp to create a local OCW.[183] Remarkably, after OC the averaged PA signal amplitude had increased by about eight times, as from individual capillaries up to 22 times with imaged vessel density increased by about 10 times.

The effect of glycerol concentration on the OR-PAM imaging contrast and probing depth was also investigated on fresh abdominal porcine skin samples of 0.5 mm in thickness covering a phantom light absorber.[289] The PA signal amplitude increases on 8.1%, 76%, and 165% for application of 20%, 40%, and 60% glycerol, respectively.

In the clinical research, OC method for the first time was shown as a beneficial technology for significant improvement of PA flow cytometry (PAFC) of circulating tumor cells in deep blood vessels in humans.[288] Using 99% glycerol, the feasibility of PA contrast improvement was demonstrated for human hand veins. OC effect was achieved in about 20 min by sequent skin ethanol cleaning (2 min), microdermabrasion (4 min), glycerol application enhanced by manual massage (4 min), and sonophoresis (10 min). Using a mouse skin layer of 0.8 mm in thickness covering a blood vessel phantom, 1.6-fold decrease in laser spot blurring and similar increase in PA signal amplitude from blood background allowed for 1.7-fold increase of peak counting rate for B16F10 melanoma cells in blood flow.

Acoustic resolution PA microscopy (AR-PAM), which also suffers from the scattering of light and the attenuation of an acoustic wave caused by inhomogeneities in the structure of the tissue, proved to be of benefit from OC.[290–292] AR-PAM allows one to image the subcutaneous microvasculature with a spatial resolution of tens of micrometers. Such commonly used OCAs as PEG-400 in combination with an appropriate penetration enhancer and pure glycerol significantly improve the PA signal amplitude and image quality of deep-sealed blood vessels and shallow vessels, respectively.[290]

A combination of AR-PAM with ultrasonography allows for studies of the mechanism of OC and OCA impact on acoustical properties of tissues.[291] One system provides measurements of acoustic speed, impedance, and absorption coefficient of skin tissues and OCAs (glycerol and PEG-400). It was also demonstrated that OCA, composed of laurinol, DMSO, sorbitol, alcohol, glucose, and sodium dodecyl benzene sulfonate, and named as a skull optical clearing solution (SOCS), could enhance not only the transmittance of light through a mouse skull, but also that of ultrasound.[292] *In vivo* studies confirmed that SOCS could significantly improve cerebral microvasculature imaging by AR-PAM.

OCAs can be used as blood flushing agents for accurate diagnosing vulnerable plaques and guiding atherosclerosis treatment by combined optical and acoustic intravascular imaging systems.[198] In this work, three commonly used OCAs were investigated as potential flushing agents: mannitol, dextran, and iohexol (Omnipaque™). Testing of these OCAs in a closed-loop circulation model and *in vivo* on rabbits, it was found that a highly concentrated dextran is the most appropriate OCA for simultaneous intravascular ultrasound and OCT imaging.[198]

The enhanced delivery of OCAs [PEG and polypropylene glycol (PPG)] through skin *in vitro* at sample pretreatment by hyaluronic acid (HA) provided a significant increase of NIR light transmittance (up to 47-fold) and improvement of OA/PA image contrast.[293] This two-step technique due to action of 0.5% HA in aqueous solution during 30 min improves skin penetration for hydrophilic and lipophilic OCAs.

As we see, OA/PA signal can be significantly increased not only due to less laser beam distortion at OC, but also due to acoustical properties improvement.[291,292] *In vivo* studies for OC of mouse skulls by SOCS demonstrated a considerable enhancement of AR-PAM capability for cerebral microvasculature imaging.[292] One of the reasons for improvement of acoustic properties could be increased tissue stiffness at OCA interaction with tissue collagen inducing temporal molecular cross-linking.[294,295]

The OC is a prospective method for imaging of lymph nodes in cancer research using different optical modalities such as digital microscopy with high-resolution cameras, PA imaging, confocal microscopy, and OCT.[285,286] Topical application of 80% glycerol aqueous solution gives a possibility for the label-free imaging of a fresh lymph node at the cellular level together with surrounding microstructures. PA cell mapping enhanced by OC will allow one to quantify distribution and number of melanoma metastases in sentinel lymph nodes through transparent skin.[286,288]

OCAs and their components also may serve as testing agents due to their mainly reversible impact on optical and acoustical properties of tissues. The feasibility of PA imaging and characterization of bone aiming clinical management of osteoporosis and other bone diseases was recently demonstrated for bovine ribs before and after their treatment by EDTA.[296]

13 Conclusion

Recent technological advances in photonics have caused tremendous progress in the development of innovative methods and systems for clinical functional optical imaging, laser surgery, and phototherapy. Intensive research and development of the biomedical optical methods and techniques have stimulated a great interest in quantification of optical properties of tissues. The requirements for a significant increase in the effectiveness of optical sensing techniques and deep light delivery for therapeutic purposes also strongly stimulate interest in the development of OC technologies that are suitable for *in vivo* applications. Some of these technologies are demonstrated in this paper.

Disclosures

No conflicts of interest, financial or otherwise, are declared by the authors.

Acknowledgments

This study was supported in part by the RFBR Grant Nos. 17-02-00358, 17-32-50190 for young researchers, 17-00-00186, 17-00-00275 (K), 18-52-16025, 18-32-00587, and 18-32-00202; the RF MES Grant Nos. 3.1586.2017/4.6 and 17.1223.2017/AP; Scholarships of the President of the RF for young researchers SP-3507.2018.4, the RF Governmental Grant No. 14.Z50.31.0044, and Russian Science Foundation (RSF) Grant No. 18-12-00328. The authors are thankful to Alla Bucharskaya, Ekaterina Galanzha, Kirill Larin, Martin Leahy, Luis Oliveira, Oxana Semyachkina-Glushkovskaya, Vladimir Zharov, and Dan Zhu for their cooperation.

References

1. L. V. Wang and H. Wu, *Biomedical Optics: Principles and Imaging*, John Wiley and Sons, Inc., Hoboken, New Jersey (2007).
2. I. V. Turchin, "Methods of biomedical optical imaging: from subcellular structures to tissues and organs," *Phys. Uspekhi* **59**, 487–501 (2016).
3. J. Huang et al., "Second derivative multispectral algorithm for quantitative assessment of cutaneous tissue oxygenation," *J. Biomed. Opt.* **20**(3), 036001 (2015).
4. A. Holmer et al., "Oxygenation and perfusion monitoring with a hyperspectral camera system for chemical based tissue analysis of skin and organs," *Physiol. Meas.* **37**, 2064–2078 (2016).
5. S. A. Boppart et al., "Label-free optical imaging technologies for rapid translation and use during intraoperative surgical and tumor margin assessment," *J. Biomed. Opt.* **23**(2), 021104 (2018).
6. X. Chen et al., "*In vivo* real-time imaging of cutaneous hemoglobin concentration, oxygen saturation, scattering properties, melanin content, and epidermal thickness with visible spatially modulated light," *Biomed. Opt. Express* **8**(12), 5468–5482 (2017).
7. K. V. Larin et al., "Optical clearing for OCT image enhancement and in-depth monitoring of molecular diffusion," *IEEE J. Sel. Top. Quantum. Electron.* **18**(3), 1244–1259 (2012).
8. R. Ankri et al., "In-vivo tumor detection using diffusion reflection measurements of targeted gold nanorods—a quantitative study," *J. Biophotonics* **5**(3), 263–273 (2012).
9. E. Angell-Petersen, H. Hirschberg, and S. J. Madsen, "Determination of fluence rate and temperature distributions in the rat brain; implications for photodynamic therapy," *J. Biomed. Opt.* **12**(1), 014003 (2007).
10. S. Kim and S. Jeong, "Effects of temperature-dependent optical properties on the fluence rate and temperature of biological tissue during low-level laser therapy," *Lasers Med. Sci.* **29**, 637–644 (2014).
11. Y. Ren et al., "Thermal dosage investigation for optimal temperature distribution in gold nanoparticle enhanced photothermal therapy," *Int. J. Heat Mass Transfer* **106**, 212–221 (2017).
12. G. Terentyuk et al., "Gold nanorods with a hematoporphyrin-loaded silica shell for dual-modality photodynamic and photothermal treatment of tumors *in vivo*," *Nano Res.* **7**(3), 325–337 (2014).
13. L. A. Dombrovsky, "A new method to retrieve spectral absorption coefficient of highly-scattering and weakly-absorbing materials," *J. Quantum. Spectr. Radiative Transfer* **172**, 75–82 (2016).
14. Q. Fang and X.-H. Hu, "Modeling of skin tissue ablation by nanosecond pulses from ultraviolet to near-infrared and comparison with experimental results," *IEEE J. Quantum Electron.* **40**(1), 69–77 (2004).
15. L. C. L. Chin, W. M. Whelan, and I. A. Vitkin, "Perturbative diffusion theory formalism for interpreting temporal light intensity changes during laser interstitial thermal therapy," *Phys. Med. Biol.* **52**, 1659–1674 (2007).
16. N. Sapogova et al., "Model for indirect laser surgery," *Biomed. Opt. Express* **8**(1), 104–111 (2017).
17. V. V. Tuchin, *Tissue Optics: Light Scattering Methods and Instruments for Medical Diagnostics*, 3rd ed., Vol. **PM 254**, p. 988, SPIE Press, Bellingham, Washington (2015).
18. W.-F. Cheong, S. A. Prahl, and A. J. Welch, "A review of the optical properties of biological tissue," *IEEE J. Quantum Electronics* **26**(12), 2166–2185 (1990).
19. A. J. Welch and M. J. C. van Gemert, *Optical-Thermal Response of Laser-Irradiated Tissue*, 2nd ed., Springer, Heidelberg (2011).
20. J. Mobley, T. Vo-Dinh, and V. V. Tuchin, "Optical properties of tissues," Chapter 2 in *Biomedical Photonics Handbook*, T. Vo-Dinh, Ed., pp. 23–122, Taylor & Francis Group, LLC, CRC Press Inc., Boca Raton, Florida (2015).
21. A. N. Bashkatov, E. A. Genina, and V. V. Tuchin, "Tissue optical properties," Chapter 5 in *Handbook of Biomedical Optics*, D. A. Boas, C. Pitris, and N. Ramanujam, Eds., pp. 67–100, Taylor & Francis Group, LLC, CRC Press Inc., Boca Raton, Florida (2011).
22. J. L. Sandell and T. C. Zhu, "A review of in-vivo optical properties of human tissues and its impact on PDT," *J. Biophotonics* **4**(11–12), 773–787 (2011).
23. A. N. Bashkatov, E. A. Genina, and V. V. Tuchin, "Optical properties of skin, subcutaneous, and muscle tissues: a review," *J. Innov. Opt. Health Sci.* **4**(1), 9–38 (2011).
24. S. L. Jacques, "Optical properties of biological tissues: a review," *Phys. Med. Biol.* **58**, R37–R61 (2013).
25. N. Bosschaart et al., "A literature review and novel theoretical approach on the optical properties of whole blood," *Lasers Med. Sci.* **29**, 453–479 (2014)
26. A. N. Bashkatov et al., "Optical properties of human skin, subcutaneous and mucous tissues in the wavelength range from 400 to 2000 nm," *J. Phys. D: Appl. Phys.* **38**, 2543–2555 (2005).
27. S. L. Jacques, "How tissue optics affect dosimetry of photodynamic therapy," *J. Biomed. Opt.* **15**(5), 051608 (2010).
28. C. Holmer et al., "Colorectal tumors and hepatic metastases differ in their optical properties—relevance for dosimetry in laser-induced interstitial thermotherapy," *Lasers Surg. Med.* **38**, 296–304 (2006).
29. F. Stelzle et al., "Diffuse reflectance spectroscopy for optical soft tissue differentiation as remote feedback control for tissue-specific laser surgery," *Lasers Surg. Med.* **42**, 319–325 (2010).
30. R. K. Wang and V. V. Tuchin, *Advanced Biophotonics. Tissue Optical Sectioning*, Taylor & Francis Group LLC, CRC Press, Boca Raton, Florida (2014).
31. M. R. Hamblin, P. Avci, and G. K. Gupta, *Imaging in Dermatology*, Elsevier Inc., London (2016).
32. V. V. Tuchin, *Handbook of Optical Biomedical Diagnostics*, 2nd ed., SPIE Press, Bellingham, Washington (2016).
33. L. Shi and R. R. Alfano, *Deep Imaging in Tissue and Biomedical Materials: Using Linear and Nonlinear Optical Methods*, Taylor & Francis Group, Pan Stanford Publishing Pte. Ltd., Singapore (2017).
34. S. J. Madsen, *Optical Methods and Instrumentation in Brain Imaging and Therapy*, Springer, New York (2013).
35. G. Lu and B. Fei, "Medical hyperspectral imaging: a review," *J. Biomed. Opt.* **19**(1), 010901 (2014).
36. Y. Engelborghs and A. J. W. G. Visser, *Fluorescence spectroscopy. Methods and Protocols*, Springer Science + Business Media, Heidelberg (2014).
37. Y. Hoshi and Y. Yamada, "Overview of diffuse optical tomography and its clinical applications," *J. Biomed. Opt.* **21**(9), 091312 (2016).
38. R. Salzer and H. W. Siesler, *Infrared and Raman Spectroscopic Imaging*, Wiley-VCH Verlag & Co. KGaA, Weinheim (2014).
39. D. Grosenick et al., "Review of optical breast imaging and spectroscopy," *J. Biomed. Opt.* **21**(9), 091311 (2016).
40. M. Y. Kirillin et al., "Contrasting properties of gold nanoshells and titanium dioxide nanoparticles for OCT imaging of skin: Monte Carlo simulations and *in vivo* study," *J. Biomed. Opt.* **14**(2), 021017 (2009).
41. A. Haeberlin et al., "The first batteryless, solar-powered cardiac pacemaker," *Heart Rhythm* **12**, 1317–1323 (2015).
42. A. I. Chen et al., "Multilayered tissue mimicking skin and vessel phantoms with tunable mechanical, optical, and acoustic properties," *Med. Phys.* **43**(6), 3117–3131 (2016).
43. P. Lemaillet, J.-P. Bouchard, and D. W. Allen, "Development of traceable measurement of the diffuse optical properties of solid reference standards for biomedical optics at National Institute of Standards and Technology," *Appl. Opt.* **54**(19), 6118–6127 (2015).
44. M. S. Wrobel et al., "Use of optical skin phantoms for preclinical evaluation of laser efficiency for skin lesion therapy," *J. Biomed. Opt.* **20**(8), 085003 (2015).
45. A. D. Krainov et al., "Optical properties of mouse biotissues and their optical phantoms," *Opt. Spectrosc.* **115**(2), 193–200 (2013).

46. D. A. Loginova et al., "Liquid optical phantoms mimicking spectral characteristics of laboratory mouse biotissue," *Quantum Electron.* **46**(6), 528–533 (2016).
47. N. Kollias, I. Seo, and P. R. Bargo, "Interpreting diffuse reflectance for in vivo skin reactions in terms of chromophores," *J. Biophotonics* **3**(1–2), 15–24 (2010).
48. R. Nachabe et al., "Estimation of biological chromophores using diffuse optical spectroscopy: benefit of extending the UV-VIS wavelength range to include 1000 to 1600 nm," *Opt. Express* **1**(24), 1432–1442 (2010).
49. A. Bhandari et al., "Modeling optical properties of human skin using Mie theory for particles with different size distribution and refractive index," *Opt. Express* **19**(15), 14549–14567 (2011).
50. D. H. P. Schneiderheinze, T. R. Hillman, and D. D. Sampson, "Modified discrete particle model of optical scattering in skin tissue accounting for multiparticle scattering," *Opt. Express* **15**(23), 15002–15010 (2007).
51. A. Bjorgan, M. Milanic, and L. L. Randeberg, "Estimation of skin optical parameters for real-time hyperspectral imaging applications," *J. Biomed. Opt.* **19**(6), 066003 (2014).
52. D. Yudovsky and L. Pilon, "Retrieving skin properties from in vivo spectral reflectance measurements," *J. Biophotonics* **4**(5), 305–314 (2011).
53. V. V. Tuchin, *Optical Clearing of Tissues and Blood*, SPIE Press, Bellingham, Washington (2006).
54. E. A. Genina et al., "Optical clearing of tissues: benefits for biology, medical diagnostics and phototherapy," Chapter 10 in *Handbook on Optical Biomedical Diagnostics, Vol. 2: Methods*, 2nd ed., V. V. Tuchin, Ed., pp. 565–937, SPIE Press, Bellingham, Washington (2016).
55. D. Zhu et al., "Recent progress in tissue optical clearing," *Laser Photonics Rev.* **7**(5), 732–757 (2013).
56. E. A. Genina, A. N. Bashkatov, and V. V. Tuchin, "Tissue optical immersion clearing," *Expert Rev. Med. Devices* **7**, 825–842 (2010).
57. E. A. Genina et al., "Light-tissue interaction at optical clearing," Chapter 7 in *Laser Imaging and Manipulation in Cell Biology*, F. S. Pavone, Ed., pp. 115–164, Wiley-VCH Verlag GmbH & Co. KGaA, Weinheim, Germany (2010).
58. M. Y. Kirillin, P. D. Agrba, and V. A. Kamensky, "*In vivo* study of the effect of mechanical compression on formation of OCT images of human skin," *J. Biophotonics* **3**(12), 752–758 (2010).
59. A. M. Smith, M. C. Mancini, and S. Nie, "Second window for *in vivo* imaging," *Nat. Nanotechnol.* **4**, 710–711 (2009).
60. L. Shi et al., "Transmission in near-infrared optical windows for deep brain imaging," *J. Biophotonics* **9**(1–2), 38–43 (2016).
61. A. N. Bashkatov et al., "Optical properties of peritoneal biological tissues in the spectral range of 350–2500 nm," *Opt. Spectrosc.* **120**(1), 1–8 (2016).
62. D.-K. Yao et al., "Optimal ultraviolet wavelength for *in vivo* photoacoustic imaging of cell nuclei," *J. Biomed. Opt.* **17**(5), 056004 (2012).
63. T. E. Renkoski et al., "Ratio images and ultraviolet C excitation in autofluorescence imaging of neoplasms of the human colon," *J. Biomed. Opt.* **18**(1), 016005 (2013).
64. A. Schönhals et al., "Optical properties of porcine dermis in the mid-infrared absorption band of glucose," *Analyst* **142**, 1235–1243 (2017).
65. A. P. M. Michel et al., "*In vivo* measurement of mid-infrared light scattering from human skin," *Biomed. Opt. Express* **4**(4), 520–530 (2013).
66. W. Petrich, "Mid-infrared and Raman spectroscopy for medical diagnostics," *Appl. Spectrosc. Rev.* **36**(2–3), 181–237 (2001).
67. C. S. Joseph et al., "Imaging of ex vivo nonmelanoma skin cancers in the optical and terahertz spectral regions," *J. Biophotonics* **7**(5), 295–303 (2014).
68. K.-E. Peiponen, J. A. Zeitler, and M. Kuwata-Gonokami, Eds., *Terahertz Spectroscopy and Imaging*, Springer-Verlag, Berlin Heidelberg (2013).
69. A. Lopez-Maestresalas et al., "Bulk optical properties of potato flesh in the 500-1900 nm range," *Food Bioprocess Technol.* **9**, 463–470 (2016).
70. J. J. Xia et al., "Characterizing beef muscles with optical scattering and absorption coefficients in VIS-NIR region," *Meat Sci.* **75**, 78–83 (2007).
71. R. Lu, Ed., *Light Scattering Technology for Food Property, Quality and Safety Assessment*, Taylor & Francis Group, LLC, Boca Raton, Florida (2016).
72. E. Zamora-Rojas et al., "Prediction of fatty acids content in pig adipose tissue by near infrared spectroscopy: at-line versus in-situ analysis," *Meat Sci.* **95**, 503–511 (2013).
73. A. N. Bashkatov et al., "Optical properties of the subcutaneous adipose tissue in the spectral range 400–2500 nm," *Opt. Spectrosc.* **99**(5), 836–842 (2005).
74. A. N. Bashkatov et al., "Optical properties of human cranial bone in the spectral range from 800 to 2000 nm," *Proc. SPIE* **6163**, 616310–616310-11 (2006).
75. A. N. Bashkatov et al., "Optical properties of human stomach mucosa in the spectral range from 400 to 2000 nm: prognosis for gastroenterology," *Med. Laser Appl.* **22**, 95–104 (2007).
76. A. N. Bashkatov et al., "Optical properties of human colon tissues in the 350–2500 nm spectral range," *Quantum Electron.* **44**(8), 779–784 (2014).
77. A. N. Bashkatov et al., "Optical properties of human sclera in spectral range 370–2500 nm," *Opt. Spectrosc.* **109**(2), 197–204 (2010).
78. E. A. Genina et al., "Optical clearing of human dura mater," *Opt. Spectrosc.* **98**(3), 470–476 (2005).
79. S. A. Prahl, M. J. C. van Gemert, and A. J. Welch, "Determining the optical properties of turbid media by using the adding-doubling method," *Appl. Opt.* **32**(4), 559–568 (1993).
80. M. DiGirolamo and J. L. Owens, "Water content of rat adipose tissue and isolated adipocytes in relation to cell size," *Am. J. Physiol.* **231**(5), 1568–1572 (1976).
81. D. Levitz et al., "Determination of optical scattering properties of highly-scattering media in optical coherence tomography images," *Opt. Express* **12**(2), 249–259 (2004).
82. D. J. Faber et al., "Quantitative measurement of attenuation coefficients of weakly scattering media using optical coherence tomography," *Opt. Express* **12**(19), 4353–4365 (2004).
83. I. V. Turchin et al., "Novel algorithm of processing optical coherence tomography images for differentiation of biological tissue pathologies," *J. Biomed. Opt.* **10**(6), 064024 (2005).
84. S. Carvalho et al., "Wavelength dependence of the refractive index of human colorectal tissues: comparison between healthy mucosa and cancer," *J. Biomed. Photon. Eng.* **2**(4), 040307 (2016).
85. P. Giannios et al., "Complex refractive index of normal and malignant human colorectal tissue in the visible and near-infrared," *J. Biophotonics* **10**(2), 303–310 (2017).
86. A. M. Zysk, E. J. Chaney, and S. A. Boppart, "Refractive index of carcinogen-induced rat mammary tumours," *Phys. Med. Biol.* **51**, 2165–2177 (2006).
87. O. S. Zhernovaya, V. V. Tuchin, and I. V. Meglinski, "Monitoring of blood proteins glycation by refractive index and spectral measurements," *Laser Phys. Lett.* **5**(6), 460–464 (2008).
88. O. Sydoruk et al., "Refractive index of solutions of human hemoglobin from the near-infrared to the ultraviolet range: Kramers–Kronig analysis," *J. Biomed. Opt.* **17**(11), 115002 (2012).
89. J. J. J. Dirckx, L. C. Kuypers, and W. F. Decraemer, "Refractive index of tissue measured with confocal microscopy," *J. Biomed. Opt.* **10**(4), 044014 (2005).
90. F. P. Bolin et al., "Refractive index of some mammalian tissues using a fiber optic cladding method," *Appl. Opt.* **28**(12), 2297–2303 (1989).
91. M. Daimon and A. Masumura, "Measurement of the refractive index of distilled water from the near-infrared region to the ultraviolet region," *Appl. Opt.* **46**(18), 3811–3820 (2007).
92. D. K. Sardar and L. B. Levy, "Optical properties of whole blood," *Lasers Med. Sci.* **13**(2), 106–111 (1998).
93. G. J. Tearney et al., "Determination of the refractive index of highly scattering human tissue by optical coherence tomography," *Opt. Lett.* **20**, 2258–2260 (1995).
94. M. Ohmi et al., "In vitro simultaneous measurement of refractive index and thickness of biological tissue by the low coherence interferometry," *IEEE Trans. Biomed. Eng.* **47**, 1266–1270 (2000).
95. V. V. Tuchin, X. Xu, and R. K. Wang, "Dynamic optical coherence tomography in optical clearing, sedimentation and aggregation study of immersed blood," *Appl. Opt.* **41**(1), 258–271 (2002).
96. X. Wang et al., "Simultaneous refractive index and thickness measurement of biotissue by optical coherence tomography," *J. Biomed. Opt.* **7**, 628–632 (2002).

97. A. V. Zvyagin et al., "Refractive index tomography of turbid media by bifocal optical coherence refractometry," *Opt. Express* **11**, 3503–3517 (2003).
98. A. Knüttel, S. Bonev, and W. Knaak, "New method for evaluation of *in vivo* scattering and refractive index properties obtained with optical coherence tomography," *J. Biomed. Opt.* **9**(2), 265–273 (2004).
99. A. M. Zysk et al., "Needle-based refractive index measurement using low-coherence interferometry," *Opt. Lett.* **32**, 385–387 (2007).
100. H.-C. Cheng and Y.-C. Liu, "Simultaneous measurement of group refractive index and thickness of optical samples using optical coherence tomography," *Appl. Opt.* **49**, 790–797 (2010).
101. I. Y. Yanina, N. A. Trunina, and V. V. Tuchin, "Photoinduced cell morphology alterations quantified within adipose tissues by spectral optical coherence tomography," *J. Biomed. Opt.* **18**(11), 111407 (2013).
102. M. Jedrzejewska-Szczerska, "Measurement of complex refractive index of human blood by low-coherence interferometry," *Eur. Phys. J. Spec. Top.* **222**, 2367–2372 (2013).
103. O. Zhernovaya et al., "The refractive index of human hemoglobin in the visible range," *Phys. Med. Biol.* **56**(13), 4013–4021 (2011).
104. Z. Deng et al., "Determination of continuous complex refractive index dispersion of biotissue based on internal reflection," *J. Biomed. Opt.* **21**(1), 015003 (2016).
105. Y. L. Jin et al., "Refractive index measurement for biomaterial samples by total internal reflection," *Phys. Med. Biol.* **51**(20), N371–N379 (2006).
106. A. García-Valenzuela and H. Contreras-Tello, "Optical model enabling the use of Abbe-type refractometers on turbid suspensions," *Opt. Lett.* **38**(5), 775–777 (2013).
107. H. Contreras-Tello and A. García-Valenzuela, "Refractive index measurement of turbid media by transmission of backscattered light near the critical angle," *Appl. Opt.* **53**(21), 4768–4778 (2014).
108. H. Sobral and M. Peña-Gomar, "Determination of the refractive index of glucose-ethanol-water mixtures using spectroscopic refractometry near the critical angle," *Appl. Opt.* **54**(28), 8453–8458 (2015).
109. G. Mazarevica, T. Freivalds, and A. Jurka, "Properties of erythrocyte light refraction in diabetic patients," *J. Biomed. Opt.* **7**(2), 244–247 (2002).
110. V. V. Tuchin, "Tissue optics and photonics: light-tissue interaction [Review]," *J. Biomed. Photon. Eng.* **1**(2), 98–134 (2015).
111. I. Y. Yanina et al., "Monitoring of temperature-mediated adipose tissue phase transitions by refractive-index measurements," *Proc. SPIE* **9421**, 94210K (2014).
112. E. N. Lazareva and V. V. Tuchin, "The temperature dependence of refractive index of hemoglobin at the wavelengths 930 and 1100 nm," *Proc. SPIE* **9917**, 99170U (2016).
113. E. N. Lazareva and V. V. Tuchin, "Measurement of refractive index of hemoglobin in the visible/NIR spectral range," *J. Biomed. Opt.* **23**(3), 1 (2018).
114. I. Y. Yanina, E. N. Lazareva, and V. V. Tuchin, "Refractive index of adipose tissue and lipid droplet measured in a wide spectral and temperature ranges," *Appl. Opt.* **57**(17), 4839–4848 (2018).
115. I. Y. Yanina et al., "Monitoring of temperature-mediated phase transitions of adipose tissue by combined optical coherence tomography and Abbe refractometry," *J. Biomed. Opt.* **23**(1), 016003 (2018).
116. E. N. Lazareva and V. V. Tuchin, "Blood refractive index modelling in the visible and near infrared spectral regions," *J. Biomed. Photon. Eng.* **4**(1), 010503 (2018).
117. F. F. de Sousa et al., "Dielectric properties of oleic acid in liquid phase," *J. Bionanosci.* **3**(2), 139–142 (2009).
118. S. Ojha, H. Budge, and M. E. Symonds, "Adipocytes in normal tissue biology," in *Pathobiology of Human Disease. A Dynamic Encyclopedia of Disease Mechanisms, Part II: Organ Systems Pathophysiology*, L. M. McManus and R. N. Mitchell, Eds., pp. 2003–2013, Elsevier, Medical, Academic Press, New York (2014).
119. R. Barer, "Refractometry and interferometry of living cells," *J. Opt. Soc. Am.* **47**(6), 545–556 (1957).
120. E. A. Genina et al., "Optical clearing of biological tissues: prospects of application in medical diagnostics and phototherapy [Review]," *J. Biomed. Photon. Eng.* **1**(1), 22–58 (2015).
121. L. M. Oliveira et al., "Skeletal muscle dispersion (400–1000 nm) and kinetics at optical clearing," *J. Biophotonics* **11**(1), e201700094 (2018).
122. D. K. Tuchina et al., "Optical clearing of skin tissue ex vivo with polyethylene glycol," *Opt. Spectrosc.* **120**(1), 28–37 (2016).
123. M. Friebel and M. Meinke, "Determination of the complex refractive index of highly concentrated hemoglobin solutions using transmittance and reflectance measurements," *J. Biomed. Opt.* **10**(6), 064019 (2005).
124. J. Gienger et al., "Determining the refractive index of human hemoglobin solutions by Kramers–Kronig relations with an improved absorption model," *Appl. Opt.* **55**(31), 8951–8961 (2016).
125. M. Yahya and M. Z. Saghir, "Empirical modelling to predict the refractive index of human blood," *Phys. Med. Biol.* **61**, 1405–1415 (2016).
126. J. Singh, *Optical Properties of Condensed Matter and Applications*, Wiley, Chichester (2006).
127. G. Popescu, *Quantitative Phase Imaging of Cells and Tissues*, McGraw-Hill, New York (2011).
128. H. Ding et al., "Optical properties of tissues quantified by Fourier-transform light scattering," *Opt. Lett.* **34**(9), 1372–1374 (2009).
129. M. Lee et al., "Label-free optical quantification of structural alterations in Alzheimer's disease," *Sci. Rep.* **6**, 31034 (2016).
130. X. Wang and L. V. Wang, "Propagation of polarized light in birefringent turbid media: a Monte Carlo study," *J. Biomed. Opt.* **7**(3), 279–290 (2002).
131. M. F. G. Wood, X. Guo, and I. A. Vitkin, "Polarized light propagation in multiply scattering media exhibiting both linear birefringence and optical activity: Monte Carlo model and experimental methodology," *J. Biomed. Opt.* **12**(1), 014029 (2007).
132. M.-R. Antonelli et al., "Mueller matrix imaging of human colon tissue for cancer diagnostics: how Monte Carlo modeling can help in the interpretation of experimental data," *Optics Express* **18**(10), 10200–10208 (2010).
133. N. Ghosh and I. A. Vitkin, "Tissue polarimetry: concepts, challenges, applications and outlook," *J. Biomed. Opt.* **16**(11), 110801 (2011).
134. Y. Guo et al., "Study on retardance due to well-ordered birefringent cylinders in anisotropic scattering media," *J. Biomed. Opt.* **19**(6), 065001 (2014).
135. D. Chen et al., "Study of optical clearing in polarization measurements by Monte Carlo simulations with anisotropic tissue-mimicking models," *J. Biomed. Opt.* **21**(8), 081209 (2016).
136. V. V. Tuchin, "Polarized light interaction with tissues," *J. Biomed. Opt.* **21**(7), 071114 (2016).
137. D. Chen et al., "Mueller matrix polarimetry for characterizing microstructural variation of nude mouse skin during tissue optical clearing," *Biomed. Opt. Express* **8**(8), 3559–3570 (2017).
138. A. A. de Aro, B. de Campos Vidal, and E. R. Pimentel, "Biochemical and anisotropical properties of tendons," *Micron* **43**(2), 205–214 (2012).
139. J. Kastelic, A. Galeski, and E. Baer, "The multicomposite structure of tendon," *Connective Tissue Res.* **6**(1), 11–23 (1978).
140. R. W. D. Rowe, "The structure of rat tail tendon," *Connect. Tissue Res.* **14**(1), 9–20 (1985).
141. P. Fratzl, *Collagen: Structure and Mechanics*, Springer, New York (2008).
142. M. E. Shvachkina et al., "Average refractive index of tendon as a function of water content," *J. Biomed. Photon. Eng.*, **4**(1), 010302 (2018).
143. Y. L. Kim et al., "Variation of corneal refractive index with hydration," *Phys. Med. Biol.* **49**(5), 859–868 (2004).
144. W. V. Sorin and D. F. Gray, "Simultaneous thickness and group index measurement using optical low-coherence reflectometry," *IEEE Photonics Technol. Lett.* **4**(1), 105–107 (1992).
145. X. J. Wang et al., "Group refractive index measurement of dry and hydrated type I collagen films using optical low-coherence reflectometry," *J. Biomed. Opt.* **1**(2), 212–217 (1996).
146. D. J. Segelstein, "The complex refractive index of water," Doctoral dissertation, University of Missouri-Kansas City, Kansas City (1981).
147. S. Kedenburg et al., "Linear refractive index and absorption measurements of nonlinear optical liquids in the visible and near-infrared spectral region," *Opt. Materials Express* **2**(11), 1588–1611 (2012).
148. E. P. Katz and S. T. Li, "Structure and function of bone collagen fibrils," *J. Mol. Biol.* **80**(1), 1–15 (1973).
149. D. W. Leonard and K. M. Meek, "Refractive indices of the collagen fibrils and extrafibrillar material of the corneal stroma," *Biophys. J.* **72**(3), 1382–1387 (1997).

150. C. Morin, C. Hellmich, and P. Henits, "Fibrillar structure and elasticity of hydrating collagen: a quantitative multiscale approach," *J. Theor. Biol.* **317**, 384–393 (2013).
151. S. Hayes et al., "The structural response of the cornea to changes in stromal hydration," *J. Royal Soc. Interface* **14**(131), 20170062 (2017).
152. K. M. Meek et al., "Synchrotron x-ray diffraction studies of the cornea, with implications for stromal hydration," *Biophysical J.* **60**(2), 467–474 (1991).
153. X. Wen et al., "Enhanced optical clearing of skin *in vivo* and optical coherence tomography in-depth imaging," *J. Biomed. Opt.* **17**(6), 066022 (2012).
154. M. G. Ghosn et al., "Monitoring of glucose permeability in monkey skin *in vivo* using optical coherence tomography," *J. Biophotonics* **3**, 25–33 (2010).
155. X. Guo et al., "*In vivo* comparison of the optical clearing efficacy of optical clearing agents in human skin by quantifying permeability using optical coherence tomography," *Photochem. Photobiol.* **87**, 734–740 (2011).
156. V. D. Genin et al., "*Ex vivo* investigation of glycerol diffusion in skin tissue," *J. Biomed. Photon. Eng.* **2**(1), 010303 (2016).
157. V. D. Genin et al., "Measurement of diffusion coefficient of propylene glycol in skin tissue," *Proc. SPIE* **9448**, 94480E (2015).
158. J. B. Segur and H. E. Oberstar, "Viscosity of glycerol and its aqueous solutions," *Ind. Eng. Chem.* **43**(9), 2117–2120 (1951).
159. B. Choi et al., "Determination of chemical agent optical clearing potential using in vitro human skin," *Lasers Surg. Med.* **36**, 72–75 (2005).
160. Dynamic Viscosity of Common Liquids. https://www.engineeringtoolbox.com/absolute-viscosity-liquids-d_1259.html.
161. D. Zhu et al., "Imaging dermal blood flow through the intact rat skin with an optical clearing method," *J. Biomed. Opt.* **15**(2), 026008 (2010).
162. "The functional properties of sugar," *Nordic Sugar*, http://www.nordicsugar.dk/fileadmin/Nordic_Sugar/Brochures_factsheet_policies_news/Download_center/Functional_properties_of_sugar_on_a_technical_level/Functional_prop_on_tech_level_uk.pdf.
163. D. K. Tuchina et al., "Ex vivo optical measurements of glucose diffusion kinetics in native and diabetic mouse skin," *J. Biophotonics* **8**(4), 332–346 (2015).
164. L. Oliveira et al., "Optical measurements of rat muscle samples under treatment with ethylene glycol and glucose," *J. Innov. Opt. Health Sci.* **6**(2), 1350012 (2013).
165. D. K. Tuchina et al., "Quantification of glucose and glycerol diffusion in myocardium," *J. Innov. Opt. Health Sci.* **8**(3), 1541006 (2015).
166. E. A. Genina, A. N. Bashkatov, and V. V. Tuchin, "Optical clearing of cranial bone," *Adv. Opt. Technol.* **2008**, 267867 (2008).
167. A. N. Bashkatov et al., "Glucose and mannitol diffusion in human dura mater," *Biophys. J.* **85**(5), 3310–3318 (2003).
168. I. M. Berke et al., "Seeing through musculoskeletal tissues: improving in situ imaging of bone and the lacunar canalicular system through optical clearing," *PLoS One* **11**(3), e0150268 (2016).
169. Z. Mao et al., "Influence of alcohols on the optical clearing effect of skin in vitro," *J. Biomed. Opt.* **13**(2), 021104 (2008).
170. J. Wang et al., "Sugar-induced skin optical clearing: from molecular dynamics simulation to experimental demonstration," *IEEE J. Sel. Top. Quantum Electron.* **20**(2), 7101007 (2014).
171. A. N. Bashkatov, E. A. Genina, and V. V. Tuchin, "Measurement of glucose diffusion coefficients in human tissues," Chapter 19 in *Handbook of Optical Sensing of Glucose in Biological Fluids and Tissues*, V. V. Tuchin, Ed., pp. 587–621, Taylor & Francis Group LLC, CRC Press, Boca Raton, Florida (2009).
172. J. E. Shaw, R. A. Sicree, and P. Z. Zimmet, "Global estimates of the prevalence of diabetes for 2010 and 2030," *Diabetes Res. Clin. Practice* **87**, 4–14 (2010).
173. J.-Y. Tseng et al., "Multiphoton spectral microscopy for imaging and quantification of tissue glycation," *Biomed. Opt. Express* **2**(2), 218–230 (2011).
174. E. Selvin et al., "Glycated hemoglobin, diabetes, and cardiovascular risk in nondiabetic adults," *The New Engl. J. Med.* **362**(9), 800–811 (2010).
175. N. I. Dikht et al., "Morphological study of the internal organs in rats with alloxan diabetes and transplanted liver tumor after intravenous injection of gold nanorods," *Russian Open Med. J.* **3**(3), 0301 (2014).
176. H. Q. Zhong et al., "Quantification of glycerol diffusion in human normal and cancer breast tissues in vitro with optical coherence tomography," *Laser Phys. Lett.* **7**(4), 315–320 (2010).
177. D. K. Tuchina et al., "Study of glycerol diffusion in skin and myocardium ex vivo under the conditions of developing alloxan-induced diabetes," *J. Biomed. Photon. Eng.* **3**(2), 020302 (2017).
178. F. Quondamatteo, "Skin and diabetes mellitus: what do we know?" *Cell Tissue Res.* **355**(1), 1–21 (2014).
179. L. M. Shevtsova et al., "Myocardium morphologic reorganization in experimental diabetes," *Vestnik Novgorod State Univ.* **2**(85), 146–150 (2015).
180. A. Rohilla and S. Ali, "Alloxan induced diabetes: mechanisms and effects," *Int. J. Res. Pharmaceut. Biomed. Sci.* **3**(2), 819–823 (2012).
181. B.-M. Kim et al., "Collagen structure and nonlinear susceptibility: effects of heat, glycation, and enzymatic cleavage on second harmonic signal intensity," *Lasers Surg. Med.* **27**, 329–335 (2000).
182. H. N. Mayrovitz, A. McClymont, and N. Pandya, "Skin tissue water assessed via tissue dielectric constant measurements in persons with and without diabetes mellitus," *Diabetes Technol. Ther.* **15**(1), 60–65 (2013).
183. E. I. Galanzha et al., "Skin backreflectance and microvascular system functioning at the action of osmotic agents," *J. Phys. D: Appl. Phys.* **36**(14), 1739–1746 (2003).
184. D. Briers et al., "Laser speckle contrast imaging: theoretical and practical limitations," *J. Biomed. Opt.* **18**(6), 066018 (2013).
185. J. D. Briers, "Laser Doppler, speckle and related techniques for blood perfusion mapping and imaging," *Physiol. Meas.* **22**, R35–R66 (2001).
186. A. K. Dunn, "Laser speckle contrast imaging of cerebral blood flow," *Ann. Biomed. Eng.* **40**(2), 367–377 (2011).
187. H. Cheng et al., "Hyperosmotic chemical agent's effect on in vivo cerebral blood flow revealed by laser speckle," *Appl. Opt.* **43**(31), 5772–5777 (2004).
188. Z. Mao et al., "Influence of glycerol with different concentration on skin optical clearing and morphological changes in vivo," *Proc. SPIE* **7278**, 72781T (2009).
189. P. A. Timoshina et al., "Study of blood microcirculation of pancreas in rats with alloxan diabetes by laser speckle contrast imaging," *J. Biomed. Photon. Eng.* **3**(2), 020301 (2017).
190. P. A. Timoshina et al., "Laser speckle contrast imaging of cerebral blood flow of newborn mice at optical clearing," *Proc. SPIE* **10336**, 1033610 (2017).
191. M. Brezinski et al., "Index matching to improve optical coherence tomography imaging through blood," *Circulation* **103**, 1999–2003 (2001).
192. V. V. Tuchin, X. Xu, and R. K. Wang, "Dynamic optical coherence tomography in studies of optical clearing, sedimentation, and aggregation of immersed blood," *Appl. Opt.* **41**, 258–271 (2002).
193. X. Xu et al., "Effect of dextran-induced changes in refractive index and aggregation on optical properties of whole blood," *Phys. Med. Biol.* **48**(9), 1205–1221 (2003).
194. V. Tuchin et al., "Theoretical study of immersion optical clearing of blood in vessels at local hemolysis," *Opt. Express* **12**, 2966–2971 (2004).
195. A. N. Bashkatov et al., "Immersion optical clearing of human blood in the visible and near infrared spectral range," *Opt. Spectrosc.* **98**(4), 638–646 (2005).
196. X. Xu, L. Yu, and Z. Chen, "Optical clearing of flowing blood using dextrans with spectral domain optical coherence tomography," *J. Biomed. Opt.* **13**(2), 021107 (2008).
197. Y. Ozaki et al., "Comparison of contrast media and low-molecular-weight dextran for frequency-domain optical coherence tomography," *Circulation J.* **76**(4), 922–927 (2012).
198. J. Li et al., "Optimal flushing agents for integrated optical and acoustic imaging systems," *J. Biomed. Opt.* **20**(5), 056005 (2015).
199. A. N. Bashkatov et al., "*In vivo* investigation of human skin optical clearing and blood microcirculation under the action of glucose solution," *Asian J. Phys.* **15**(1), 1–14 (2006).
200. G. Vargas et al., "Morphological changes in blood vessels produced by hyperosmotic agents and measured by optical coherence tomography," *Photochem. Photobiol.* **77**(5), 541–549 (2003).
201. G. Vargas, J. K. Barton, and A. J. Welch, "Use of hyperosmotic chemical agent to improve the laser treatment of cutaneous vascular lesions," *J. Biomed. Opt.* **13**(2), 021114 (2008).

202. J. Wang et al., "An innovative transparent cranial window based on skull optical clearing," *Laser Phys. Lett.* **9**(6), 469–473 (2012).
203. Y. Zhao et al., "Skull optical clearing window for in vivo imaging of the mouse cortex at synaptic resolution," *Light: Sci. Appl.* **7**, 17153 (2018).
204. J. Wang, R. Shi, and D. Zhu, "Switchable skin window induced by optical clearing method for dermal blood flow imaging," *J. Biomed. Opt.* **18**(6), 061209 (2013).
205. J. Wang et al., "Review: tissue optical clearing window for blood flow monitoring," *IEEE J. Sel. Topics Quant. Electr.* **20**(2), 6801112 (2014).
206. R. Shi et al., "Accessing to arteriovenous blood flow dynamics response using combined laser speckle contrast imaging and skin optical clearing," *Biomed. Opt. Express* **6**(6), 1977–1989 (2015).
207. R. Shi et al., "FSOCA-induced switchable footpad skin optical clearing window for blood flow and cell imaging in vivo," *J. Biophotonics* **10**(12), 1647–1656 (2017).
208. R. Shi et al., "*In vivo* imaging the motility of monocyte/macrophage during inflammation in diabetic mice," *J. Biophotonics* **11**(5), e201700205 (2018).
209. L. Guo et al., "Optical coherence tomography angiography offers comprehensive evaluation of skin optical clearing *in vivo* by quantifying optical properties and blood flow imaging simultaneously," *J. Biomed. Opt.* **21**(8), 081202 (2016).
210. W. Feng et al., "Lookup-table-based inverse model for mapping oxygen concentration of cutaneous microvessels using hyperspectral imaging," *Opt. Express* **25**(4), 3481–3495 (2017).
211. P. Höök et al., "Whole blood clot optical clearing for nondestructive 3D imaging and quantitative analysis," *Biomed. Opt. Express* **8**(8), 3671–3686 (2017).
212. O. Zhernovaya, V. V. Tuchin, and M. J. Leahy, "Blood optical clearing studied by optical coherence tomography," *J. Biomed. Opt.* **18**(2), 026014 (2013).
213. O. Zhernovaya, V. V. Tuchin, and M. J. Leahy, "Enhancement of OCT imaging by blood optical clearing in vessels—a feasibility study," *Photon. Lasers Med.* **5**(2), 151–159 (2016).
214. L. Northam and G. V. G. Baranoski, "A novel first principles approach for the estimation of the sieve factor of blood samples," *Optics Express* **18**, 7456–7469 (2010).
215. J. Hirshburg et al., "Correlation between collagen solubility and skin optical clearing using sugars," *Lasers Surg. Med.* **39**, 140–144 (2007).
216. G. Popescu et al., "Erythrocyte structure and dynamics quantified by Hilbert phase microscopy," *J. Biomed. Opt.* **10**(6), 060503 (2005).
217. C.-H. Lin, I. A. Aljuffali, and J.-Y. Fang, "Lasers as an approach for promoting drug delivery via skin," *Expert Opin. Drug Deliv.* **11**(4), 599–614 (2014).
218. Y. Shahzad et al., "Breaching the skin barrier through temperature modulations," *J. Control. Release* **202**, 1–13 (2015).
219. R. Yang et al., "Getting drugs across biological barriers," *Adv. Mater.* **29**(37), 1606596 (2017).
220. V. V. Tuchin, L. Wang, and D. A. Zimnyakov, *Optical Polarization in Biomedical Applications*, Springer, New York (2006).
221. J. F. de Boer, C. K. Hitzenberger, and Y. Yasuno, "Polarization sensitive optical coherence tomography—a review," *Biomed. Opt. Express* **8**(3), 1838–1873 (2017).
222. J. M. Bueno and M. C. Campbell, "Polarization properties of the in vitro old human crystalline lens," *Ophthal. Physiol. Opt.* **23**(2), 109–118 (2003).
223. Y. P. Sinichkin et al., "The effect of the optical anisotropy of scattering media on the polarization state of scattered light," *Opt. Spectrosc.* **101**(5), 802–810 (2006).
224. N. Ghosh, M. F. G. Wood, and I. A. Vitkin, "Polarized light assessment of complex turbid media such as biological tissues via Mueller matrix decomposition," in *Handbook of Photonics for Biomedical Science*, V. V. Tuchin, Ed., pp. 253–282, CRC Press, London (2010).
225. T. Novikova et al., "Polarimetric imaging for cancer diagnosis and staging," *Opt. Photonics News* **23**(10), 26–33 (2012).
226. A. Pierangelo et al., "Multispectral Mueller polarimetric imaging detecting residual cancer and cancer regression after neoadjuvant treatment for colorectal carcinomas," *J. Biomed. Opt.* **18**(4), 046014 (2013).
227. D. Layden, N. Ghosh, and A. Vitkin, "Quantitative polarimetry for tissue characterization and diagnosis," in *Advanced Biophotonics: Tissue Optical Sectioning*, R. K. Wang and V. V. Tuchin, Eds., pp. 73–108, CRC Press, Boca Raton (2013).
228. S. Bancelin et al., "Determination of collagen fiber orientation in histological slides using Mueller microscopy and validation by second harmonic generation imaging," *Optics Express* **22**(19), 22561–22574 (2014).
229. M. E. H. Jaspers et al., "*In vivo* polarization-sensitive optical coherence tomography of human burn scars: birefringence quantification and correspondence with histologically determined collagen density," *J. Biomed. Opt.* **22**(12), 121712 (2017).
230. Y. Dong et al., "A quantitative and non-contact technique to characterize microstructural variations of skin tissues during photo-damaging process based on Mueller matrix polarimetry," *Sci. Rep.* **7**, 14702 (2017).
231. A. B. Pravdin et al., "Mapping of optical properties of anisotropic biological tissues," *Proc. SPIE* **5695**, 303–310 (2005).
232. Y. P. Sinichkin, A. V. Spivak, and D. A. Yakovlev, "Simple parametric representations of the polarization optical properties of birefringent biological tissues in reflection polarization spectroscopy," *Opt. Spectrosc.* **107**(6), 873–883 (2009).
233. Y. P. Sinichkin, A. V. Spivak, and D. A. Yakovlev, "Effect of scattering anisotropy and material optical anisotropy of oriented fiber layers on the transmitted light polarization," *Opt. Spectrosc.* **109**(2), 169–177 (2010).
234. D. A. Yakovlev, V. G. Chigrinov, and H.-S. Kwok, *Modeling and Optimization of LCD Optical Performance*, Wiley, Chichester, UK (2015).
235. D. A. Yakovlev et al., "Polarization monitoring of structure and optical properties of the heterogeneous birefringent media: application in the study of liquid crystals and biological tissues," *Proc. SPIE* **5067**, 64–72 (2003).
236. H. He et al., "A possible quantitative Mueller matrix transformation technique for anisotropic scattering media," *Photonics Lasers Med.* **2**(2), 129–137 (2013).
237. M. Sun et al., "Probing microstructural information of anisotropic scattering media using rotation-independent polarization parameters," *Appl. Opt.* **53**(14), 2949–2955 (2014).
238. C. He et al., "Characterizing microstructures of cancerous tissues using multispectral transformed Mueller matrix polarization parameters," *Biomed. Opt. Express* **6**(8), 2934–2945 (2015).
239. N. J. Jan, K. Lathrop, and I. A. Sigal, "Collagen architecture of the posterior pole: high-resolution wide field of view visualization and analysis using polarized light microscopy posterior pole collagen architecture," *Invest. Ophthal. Vis. Sci.* **58**(2), 735–744 (2017).
240. N. J. Jan et al., "Polarization microscopy for characterizing fiber orientation of ocular tissues," *Biomed. Opt. Express* **6**(12), 4705–4718 (2015).
241. D. D. Yakovlev et al., "Quantitative mapping of collagen fiber alignment in thick tissue samples using transmission polarized-light microscopy," *J. Biomed. Opt.* **21**(7), 071111 (2016).
242. A. B. Pravdin, V. A. Spivak, and D. A. Yakovlev, "On the possibility of noninvasive polarimetric determination of glucose content in skin," *Opt. Spectrosc.* **120**(1), 45–49 (2016).
243. J. K. Pijanka et al., "Quantitative mapping of collagen fiber orientation in non-glaucoma and glaucoma posterior human sclera fiber orientation in posterior human sclera," *Invest. Ophthalm. Vis. Sci.* **53**(9), 5258–5270 (2012).
244. M. J. A. Girard et al., "Quantitative mapping of scleral fiber orientation in normal rat eyes," *Invest. Ophthalm. Vis. Sci.* **52**(13), 9684–9693 (2011).
245. P. Ellingsen et al., "Quantitative characterization of articular cartilage using Mueller matrix imaging and multiphoton microscopy," *J. Biomed. Opt.* **16**(11), 116002 (2011).
246. X. Yao et al., "Nondestructive imaging of fiber structure in articular cartilage using optical polarization tractography," *J. Biomed. Opt.* **21**(11), 116004 (2016).
247. L. Azinfar et al., "High resolution imaging of the fibrous microstructure in bovine common carotid artery using optical polarization tractography," *J. Biophotonics* **10**(2), 231–241 (2017).

248. M. E. Shvachkina et al., "Assessment of possibilities of transmission polarization mapping for the characterization of sclera macrostructure," *Saratov J. Med. Sci. Res.* **13**(2), 435–441 (2017).
249. J. M. Hirshburg, "Chemical agent induced reduction of skin light scattering," PhD Thesis, Texas A&M University (2009).
250. K. V. Berezin et al., "Molecular modeling of immersion optical clearing of biological tissues," *J. Mol. Model.* **24**(2), 45 (2018).
251. K. V. Berezin et al., "Studying the mechanism of tissue optical clearing using the method of molecular dynamics," *Proc. SPIE* **10336**, 103360J (2017).
252. E. Youn et al., "Determination of optimal glycerol concentration for optical tissue clearing," *Proc. SPIE* **8207**, 82070J (2012).
253. A. V. Belikov et al., "Temperature dynamics of the optical properties of lipids in vitro," *J. Opt. Technol.* **70**(11), 811–814 (2003).
254. A. V. Belikov, C. V. Prikhodko, and O. A. Smolyanskaya, "Study of thermo induced changes resulted in optical properties of fat tissue," *Proc. SPIE* **5066**, 207–212 (2003).
255. I. Y. Yanina, N. A. Trunina, and V. V. Tuchin, "Photoinduced cell morphology alterations quantified within adipose tissues by spectral optical coherence tomography," *J. Biomed. Opt.* **18**(11), 111407 (2013).
256. I. Y. Yanina et al., "Monitoring of temperature-mediated phase transitions of adipose tissue by combined optical coherence tomography and Abbe refractometry," *J. Biomed. Opt.* **23**(1), 016003 (2018).
257. V. V. Tuchin et al., "Fat tissue staining and photodynamic/photothermal effects," *Proc. SPIE* **7563**, 75630V (2010).
258. I. Y. Yanina et al., "The morphology of apoptosis and necrosis of fat cells after photodynamic treatment at a constant temperature in vitro," *Proc. SPIE* **7887**, 78870X (2011).
259. P. Avci et al., "Low-level laser therapy for fat layer reduction: a comprehensive review," *Lasers Surg. Med.* **45**(6), 349–357 (2013).
260. M. K. Caruso-Davis et al., "Efficacy of low-level laser therapy for body contouring and spot fat reduction," *Obesity Surg.* **21**(6), 722–729 (2011).
261. M. Wanner et al., "Effects of noninvasive, 1210 nm laser exposure on adipose tissue: results of a human pilot study," *Lasers Surg. Med.* **41**, 401–407 (2009).
262. G. B. Altshuler et al., "Extended theory of selective photothermolysis," *Lasers Surg. Med.* **29**, 416–432 (2001).
263. R. R. Anderson et al., "Selective photothermolysis of lipid a rich tissues: a free electron laser study," *Lasers Surg. Med.* **38**, 913–919 (2006).
264. M. J. Salzman, "Laser lipolysis using a 1064/1319-nm blended wavelength laser and internal temperature monitoring," *Semin. Cutan. Med. Surg.* **28**, 220–225 (2009).
265. B. R. Seckel et al., "The role of laser tunnels in laser-assisted lipolysis," *Lasers Surg. Med.* **41**(10), 728–737 (2009).
266. V. A. Doubrovskii et al., "Photoaction on cells of human adipose tissue in vitro," *Tsitologiia* **53**(5), 423–432 (2011).
267. V. V. Tuchin et al., "In vivo investigation of the immersion-liquid-induced human skin clearing dynamics," *Technical Phys. Lett.* **27**(6), 489–490 (2001).
268. V. A. Doubrovsky, I. Y. Yanina, and V. V. Tuchin, "Kinetics of changes in the coefficient of transmission of the adipose tissue *in vitro* as a result of photodynamic action," *Biophysics* **57**(1), 94–97 (2012).
269. I. Y. Yanina, V. A. Doubrovsky, and V. V. Tuchin, "Analysis of the in vitro optical characteristics of adipose tissue sensitized with indocyanine green under IR-laser irradiation," *Opt. Spectrosc.* **118**(3), 494–500 (2015).
270. I. Y. Yanina et al., "Optical image analysis of fat cells for indocyanine green mediated near-infrared laser treatment," *Laser Phys. Lett.* **8**(9), 684–690 (2011).
271. P. Schieberle et al., "Comparison of sensitizers in the photooxidation of unsaturated fatty acids and their methyl esters," *Zeitschriftfür Lebensmittel-Untersuchungund Forschung* **179**(2), 93–98 (1984).
272. S. D. Lamore et al., "The malondialdehyde-derived fluorophore DHP-lysine is a potent sensitizer of UVA-induced photooxidative stress in human skin cells," *J. Photochem. Photobiol. B: Biology* **101**(3), 251–264 (2010).
273. D. Del Rio, A. J. Stewart, and N. Pellegrini, "A review of recent studies on malondialdehyde as toxic molecule and biological marker of oxidative stress," *Nutr. Metab. Cardiovasc. Dis.* **15**, 316–328 (2005).
274. E. Engel et al., "Light-induced decomposition of indocyanine green," *Invest. Ophthalm. Vis. Sci.* **49**, 1777–1783 (2008).
275. B. C. Wilson and M. S. Patterson, "The physics, biophysics and technology of photodynamic therapy," *Phys. Med. Biol.* **53**(9), R61–R109 (2008).
276. M. Wenne, "The most transparent research," *Nat. Med.* **15**(10), 1106–1109 (2009).
277. Z. Yaqoob et al., "Optical phase conjugation for turbidity suppression in biological samples," *Nat. Photonics* **2**, 110–115 (2008).
278. M. Cui, E. J. McDowell, and C. Yang, "An in vivo study of turbidity suppression by optical phase conjugation (TSOPC) on rabbit ear," *Opt. Express* **18**, 25–30 (2010).
279. D. P. M. Gower, *Optical Phase Conjugation*, Springer-Verlag, New York (1994).
280. I. M. Vellekoop and A. P. Mosk, "Focusing coherent light through opaque strongly scattering media," *Opt. Lett.* **32**(16), 2309–2311 (2007).
281. A. P. Mosk et al., "Controlling waves in space and time for imaging and focusing in complex media," *Nat. Photonics* **6**, 283–292 (2012).
282. H. Yu et al., "Recent advances in wavefront shaping techniques for biomedical applications," *Curr. Appl. Phys.* **15**(5), 632–641 (2015).
283. H. Yu et al., "Collaborative effects of wavefront shaping and optical clearing agent in optical coherence tomography," *J. Biomed. Opt.* **21**(12), 121510 (2016).
284. S. Masoumi et al., "Estimation of beta-carotene using calibrated reflection spectroscopy method: phantom study," *J. Biomed. Opt.* (submitted).
285. R. W. Sun et al., "Current status, pitfalls and future directions in the diagnosis and therapy of lymphatic malformation," *J. Biophotonics* **11**(8), e201700124 (2018).
286. E. I. Galanzha et al., "In vivo fiber-based multicolor photoacoustic detection and photothermal purging of metastasis in sentinel lymph nodes targeted by nanoparticles," *J. Biophotonics* **2**(8–9), 528–539 (2009).
287. Y. Zhou, J. Yao, and L. V. Wang, "Optical clearing-aided photoacoustic microscopy with enhanced resolution and imaging depth," *Opt. Lett.* **38**(14), 2592–2595 (2013).
288. Y. A. Menyaev et al., "Optical clearing in photoacoustic flow cytometry," *Biomed. Opt. Express* **4**(12), 3030–3041 (2013).
289. Q. Zhao et al., "Concentration dependence of optical clearing on the enhancement of laser-scanning optical-resolution photoacoustic microscopy imaging," *J. Biomed. Opt.* **19**(3), 36019 (2014).
290. Y. Liu et al., "Optical clearing agents improve photoacoustic imaging in the optical diffusive regime," *Opt. Lett.* **38**(20), 4236–4239 (2013).
291. X. Yang et al., "Dynamic monitoring of optical clearing of skin using photoacoustic microscopy and ultrasonography," *Opt. Express* **22**(1), 1094–1104 (2014).
292. X. Yang et al., "Skull optical clearing solution for enhancing ultrasonic and photoacoustic imaging," *IEEE Trans. Med. Imaging* **35**(8), 1903–1906 (2016).
293. A. Liopo et al., "Optical clearing of skin enhanced with hyaluronic acid for increased contrast of optoacoustic imaging," *J. Biomed. Opt.* **21**(8), 081208 (2016).
294. C.-H. Liu et al., "Quantitative assessment of hyaline cartilage elasticity during optical clearing using optical coherence elastography," *Modern Technol. Med.* **7**, 44–51 (2015).
295. Y. Tanaka et al., "Irreversible optical clearing of sclera by dehydration and cross-linking," *Biomaterials* **32**(4), 1080–1090 (2011).
296. X. Wang et al., "Photoacoustic measurement of bone health: a study for clinical feasibility," in *Proc. of IEEE Int. Ultrasonics Symp. (IUS)* (2016).

Alexey N. Bashkatov is an associate professor in the Department of Optics and Biophotonics, a head of Laboratory of Biomedical Optics of Research-Educational Institute of Optics and Biophotonics at Saratov State University, and leading researcher at the Interdisciplinary Laboratory of Biophotonics of Tomsk State University. He is a coauthor of more than 250 invited and contributed publications, nine book chapters, and nine patents. His research interests include study of optical properties of tissues, spectroscopy, and modeling of light propagation in turbid media. He has 2200 HYPERLINK "javascript:void(0)" citations and HYPERLINK "javascript:void(0)" h-index 22 (WoS, April 7, 2018).

Kirill V. Berezin is a professor at the Department of Optics and Biophotonics of Saratov State University and a leading research fellow at Astrakhan State University. His research interests include molecular IR and Raman spectroscopy of organic compounds and molecular modeling of structures, spectral properties, and interactions in natural systems.

Konstantin N. Dvoretskiy is an associate professor of medical and biological physics at Saratov State Medical University. His research interests include optical clearing of biological tissues and molecular modeling.

Maria L. Chernavina is a graduate student of the Department of Optics and Biophotonics of Saratov State University. Her research interests include optical clearing of biological tissues and molecular modeling.

Elina A. Genina is an associate professor in the Department of Optics and Biophotonics at Saratov State University. She is a coauthor of more than 250 peer-reviewed publications, nine book chapters, and nine patents. Her research interests include biomedical optics, laser medicine, and development of methods for control of tissue absorption and scattering properties for medical optical diagnostics and therapy. She is a scientific secretary of International Symposium on Optics and Biophotonics (Saratov Fall Meeting). She has 2165 HYPERLINK "javascript:void(0)" citations and HYPERLINK "javascript:void(0)" h-index 22 (WoS, April 7, 2018).

Vadim D. Genin is a postgraduate student in the Department of Optics and Biophotonics of Saratov State University. He has authored more 5 peer-reviewed publications. His research interests include biomedical optics, study of optical properties of tissues, spectroscopy, development of methods for control of tissue absorption, and scattering properties for medical optical diagnostics and therapy.

Vyacheslav I. Kochubey is a professor at the Department of Optics and Biophotonics of Saratov State University. His research interests include spectroscopy, tissue optics, nanoparticles, and nanobiophotonics. He has published more than 150 peer-reviewed scientific papers.

Ekaterina N. Lazareva is an engineer of Department of Optics and Biophotonics of Saratov State University. Her research interests are in optical properties of biological tissues, especially of blood (its components) and adipose tissue, refractometry and spectroscopy of tissues, and tissue optical clearing.

Alexander B. Pravdin graduated from Chemistry Department of Moscow State University in 1979. He received his candidate of sciences (PhD) degree in physical chemistry from Moscow State University in 1990. From 1988, he works at optics department (later–Optics and biophotonics department) of Saratov State University, Saratov, Russia, where he is currently an associated professor. He lectures to students specializing in the field of physics of living systems and biological and medical photonics.

Marina E. Shvachkina received her MS degree from Saratov State University, Department of Optics and Biophotonics, where currently she is a PhD student. Her research interests include mechanical properties of collagenous tissue, UVA–riboflavin collagen cross-linking of sclera, tissue optical clearing, polarization microscopy.

Polina A. Timoshina is an assistant professor and engineer at the Department of Optics and Biophotonics at Saratov State University. She obtained her PhD in biophysics in 2016. She is a coauthor of 21 publications. Her research interests include tissue optics, laser medicine, tissue optical clearing, and speckle contrast imaging.

Daria K. Tuchina is an assistant professor at the Department of Optics and Biophotonics at Saratov State University. She obtained her PhD in biophysics in 2016. Her researches are focused on tissue optical clearing, investigation of diabetic tissues, and quantification of diffusion of chemical agents in tissues. She is a coauthor of 35 publications, more than 60 reports, two patents, and participant of more than 25 scientific projects, secretary of the Internet Biophotonics Conference of Saratov Fall Meeting.

Dmitry D. Yakovlev received his MS degree from Saratov State University, Saratov, Russia. Currently, he is a PhD student at the Department of Optics and Biophotonics at Saratov State University. His current research interests include polarized-light microscopy, photonics, optics of anisotropic media, and optics of biological tissues.

Dmitry A. Yakovlev is a senior researcher at the Research Educational Institute of Optics and Biophotonics, Saratov State University. He received his MS degree in physics and PhD in optics from Saratov State University in 1985 and 1998, respectively. He is the author of more than 40 journal papers and one book. His current research interests include optics of anisotropic media, biomedical optics, polarization optics, microscopy, and physics of liquid crystals.

Irina Yu. Yanina received her PhD in biophysics from Saratov State University (SSU), Saratov, Russia, in 2013. She is authored 17 papers in peer-reviewed journals and 18 papers in conference proceedings. From 2010 to present, she is an associate fellow researcher of Research-Educational Institute of Optics and Biophotonics at SSU and since 2015 is an associate professor of Department of Optics and Biophotonics of SSU. Her research interests include the development of optical methods of fat tissue destructive engineering, photodynamic/photothermal therapy, biomedical optics, drug delivery, spectroscopy and imaging in biomedicine, and optical and laser measurements.

Olga S. Zhernovaya received her MSc degree in physics (with a major in biomedical optics) from Saratov State University, Russia, in 2005, and her PhD in physics from the University of Limerick, Ireland, in 2015. Her research interests are focused on optical clearing of blood and tissues, and spectrometry and refractometry of blood and its components.

Valery V. Tuchin is a professor and head of optics and biophotonics at Saratov State University (National Research University of Russia) and several other universities. His research interests include tissue optics, laser medicine, tissue optical clearing, and nanobiophotonics. He is a fellow of SPIE and OSA, has been awarded Honored Science Worker of the Russia, Honored Professor of Saratov University, SPIE Educator Award, FiDiPro (Finland), Chime Bell Prize of Hubei Province (China), and Joseph W. Goodman Book Writing Award (OSA/SPIE). He has 20393 citations and h-index 66 (Google Scholar, August 8, 2018).